A Multi-Scale Modeling of Confined Fluid: from Nanopore to Unconventional Reservoir Simulation

Nicolas Sobecki [a],[*], Shihao Wang [b], Didier Yu Ding [a], Carlos Nieto-Draghi [a], Yu-Shu Wu [b]

[a] IFP Energies nouvelles 1 & 4, avenue de Bois-Preau 92852 Rueil-Malmaison Cedex, France
[b] Petroleum Engineering Department, Colorado School of Mines, Golden, CO 80401, USA

ARTICLE INFO

ABSTRACT

Tight oil and shale gas reservoirs have a significant part of their pore volume occupied by micro (below 2 nm) and mesopores (between 2 and 50 nm). This kind of environment creates strong interaction forces in the confined fluid with pore walls and then changes dramatically the fluid phase behavior. An important work has therefore to be done on thermodynamic modeling of the confined fluid and on developing upscaling methodology of the pore size distribution for large scale reservoir simulations. Firstly, the comparison between molecular simulation results and commonly used modified equation of state (EOS) in the literature highlighted the model of flash with capillary pressure and critical temperature and pressure shift as the best one to model confined fluid behavior. Then, fine grid matrix/fracture simulations have been built and performed for different pore size distributions. The study has shown that the pore size distribution has an important impact on reservoir production and this impact is highly dependent on the volume fraction of nanopores inside the matrix. Afterwards, coarse grid upscaling models have then been performed on the same synthetic case and compared to the reference fine grid results. The commonly used upscaling methodology of dual porosity model with average pore radius for the pore size distribution is unable to match the fine grid results. A new triple porosity model considering fracture, small pores and large pores with their own capillary pressure and EOS, together with MINC (Multiple Interacting Continua) approach, has shown very good agreement with the reference fine grid results. Finally a large scale stimulated reservoir volume with different pore size distribution inside the matrix has been built using the upscaling method developed here.

1. Introduction

World energy demand is projected to increase by 30% in 2035 (BP, 2017). According to predictions, fossil fuel will still represent more than three-quarters of world energy consumption through 2040 (U.S. Energy Information Administration, 2017). Among oil and gas production, unconventional resources such as shale gas and tight oil have emerged in the past decade as a significant solution for the petroleum industry to meet future world energy demand. Indeed they will reach together nearly thirty percent of global liquids supply by 2040 (Exxon-Mobil, 2018). Tight oil production will more than double from 2015 to 2040 (U.S. Energy Information Administration, 2016) and shale production will account for around sixty percent of the increase in gas supplies to 2035 according to BP (2017).

The flow dynamics and the fluid behavior in shale gas and tight oil reservoirs are much more complex than those in conventional reservoirs. The stimulation of the matrix by multi stage hydraulic fracturing generates a highly heterogeneous porous/fractured rock where flow occurs between an extremely low permeability matrix with nanopores and the fracture up to the well. The modeling of the matrix/fracture exchange in such reservoirs becomes therefore a challenge in terms of flow and phase behavior. An accurate modeling is therefore crucial for optimal production forecasts, which are currently very challenging especially for the Gas–Oil-Ratio (GOR) prediction (Kumar et al., 2013; Nojabaei et al., 2013; Tian et al., 2013). Thus this work is aimed to model thermodynamic behavior of a confined fluid inside nanometric pores using molecular simulation results as reference for the calibration of a modified Equation of State (EOS). This new pore radius dependent EOS will then be used in a triple porosity model to take into account the pore size distribution for reservoir simulations.

Tight oil and shale gas reservoirs consist of a very heterogeneous pore size distribution ranging from several nanometers to micro meters contrary to conventional reservoirs where pore size distribution has a micrometer scale. The part of micropores (below 2 nm) and mesopores (between 2 and 50 nm) can reach more than 20% of the volume

---

* Corresponding author.
  E-mail addresses: sobecki.nicolas@gmail.com (N. Sobecki), didier-yu.ding@ifp.fr (D.Y. Ding).

distribution (Kuila and Prasad, 2011). They are mainly associated with clay minerals and kerogen (Pommer, 2014). Hydrocarbon molecules range between 0.5 and 10 nm (Nelson, 2009), then interaction forces between confined fluid and pore wall molecules can become as significant as inter molecular interactions within the confined fluid. Therefore confinement changes dramatically the fluid phase behavior. Several approaches have been used to study the confinement effect in the phase behavior of confined fluids.

Firstly some nanofluidic experiments are showing that the bubble point temperature increases in nano-channels compared to the bulk fluid (Wang et al., 2014; Alfi et al., 2016a). Luo et al. (2016) and Cho et al. (2017) conducted the same kind of experiments on pore glasses and mesoporous materials respectively and measured also an increase of bubble point temperature compared to the bulk fluid.

Secondly a great deal of work has been done on extension of EOS for confined fluid behavior modeling. The modification of the thermodynamic flash by including the capillary pressure represents the first main method used in the literature (Firincioglu et al., 2012; Alharthy et al., 2013; Teklu et al., 2014; Rezaveisi et al., 2015; Xiong et al., 2015; Sandoval et al., 2016; Stimpson and Barrufet, 2016; Zhang et al., 2016a; Haider and Aziz, 2017; Lopez Jimenez et al., 2018). This method is improved by some authors by considering the thickness of the adsorbed layer (Dong et al., 2016a; Li et al., 2016). The second main method used in the literature considers a shift of critical temperature and pressure proportional of pore radius in the flash calculation (Devegowda et al., 2012; Dong et al., 2016a; Alharthy et al., 2013; Jin et al., 2013; Sanaei et al., 2014; Teklu et al., 2014; Haider and Aziz, 2017; Lopez Jimenez et al., 2018). The correlations used for critical temperature and pressure values versus pore radius are either analytical (Meyra et al., 2005) or build from molecular simulation results (Jin et al., 2013; Sanaei et al., 2014). The two methods of flash with capillary pressure and flash with shift of critical properties are also applied together (Teklu et al., 2014; Dong et al., 2016b; Lopez Jimenez et al., 2018; Zuo et al., 2018). The pore/fluid interaction effect has also been included by some authors to build a new EOS. However interaction parameters must be fitted with experimental or molecular simulation results (Travalloni et al., 2010, 2014; Barbosa et al., 2016; Islam and Sun, 2017; Luo et al., 2019).

Finally molecular simulation appears to be the most accurate and reliable method to approach the reality of the thermophysics of confined fluids. Pitakbunkate et al. (2016, 2017) have applied Grand Canonical Monte Carlo ensemble (GCMC) to methane/ethane mixture phase behavior calculation. Jin et al. (2017) modified the GCMC ensemble to create the gauge-GCMC method and studied pure system, binary and ternary system. The Gibbs Ensemble Monte Carlo (GEMC) Panagiotopoulos (1987b,a) has been widely used for confined pure fluid (Panagiotopoulos et al., 1988; Jiang and Gubbins, 1995; Gelb et al., 1999) but less work have been done for mixtures (Pathak et al., 2017; Li et al., 2012; Bi and Nasrabadi, 2019). Sobecki et al. (2019) proposed a new methodology and worflow in the Gibbs ensemble in order to model the confined fluid properties and pressures of vapor and liquid phases at equilibrium for several pure components and mixtures. Whatever the ensemble used, the observations are the same for all authors cited above. The confinement causes a shift of critical temperature and pressure of the fluid from their bulk value and vapor density increases while liquid density decreases.

All the methods cited above aim to model the confined fluid PVT for a given pore radius. The study of the impact of fluid confinement on reservoir production has been carried out by several authors for a constant pore radius value. Some authors ran reservoir simulations with capillary pressure effect on the phase behavior (Firincioglu et al., 2012; Nojabaei et al., 2013; Xiong et al., 2015; Haider and Aziz, 2017). They all studied oil system and showed that oil production is increased and gas production is decreased. Others authors chose the flash with critical point shift method (Devegowda et al., 2012; Alharthy et al., 2013; Sanaei et al., 2014; Haider and Aziz, 2017; Lopez Jimenez et al.,

2018) and showed that oil and gas production is increased regardless of fluid type.

However the pore network is in reality very complex and the reservoir has an important heterogeneity of pore sizes. Upscaling methodologies must therefore be developed in order to perform large scale reservoir simulations. Few authors have applied the pore size distribution in their model and most of them have considered an average pore radius inside a simulation cell (Firincioglu et al., 2013; Sanaei et al., 2014; Alharthy et al., 2017; Haider and Aziz, 2017; Lopez Jimenez et al., 2018) using single or double porosity model. Others authors considered the pore size distribution using the J Leverett functions or an effective radius function of the saturation of the wetting fluid. Li et al. (2016), Li and Mezzatesta (2017), Nojabaei et al. (2013), Wang et al. (2013), Xiong et al. (2015). These two methods are quite similar and seem not to be efficient. As the percentage of micro and meso pores inside shale matrix is low, the effective radius value stays quite high (or low J Leverett function value) for a large range of wetting phase saturation during the flow simulation. Then the impact of confinement is very low and the fluid behaves like bulk. Alfi et al. (2017) proposed a triple porosity method with three permeability, three porosity model to account for filtration effect in shale reservoirs. The porous media is divided into three different sub-media: fracture, large pores and small pores. Peng–Robinson EOS is used for flash calculation in large pores and fractures and a modified Peng–Robinson equation of state (Travalloni et al., 2014) is used for small pores for a specific radius in order to account for confinement effect. The two EOS must be solved simultaneously. All fugacities must be equal at equilibrium in both phases for the both sub media (large and small pores) for every component. This method is interesting but seems to be very CPU time consuming and no clear details are given on the thermodynamic equilibrium calculation and how to model the flux between sub-grids. Besides, we are not sure if the thermodynamic equilibrium between small and large pores is predominant comparing to other effects such as capillarity during a dynamic flow simulation.

The two common methods to model confined fluid PVT behavior, that is, flash with capillary pressure and flash with critical point shift, have already been compared to some experimental and Density-Functional Theory reference data (Alfi et al., 2016b; Liu et al., 2018). But to our knowledge, no works have already be done using reliable and exhaustive results of different thermodynamical properties from Gibbs molecular simulation as reference data. In this paper, molecular simulation results for liquid/vapor equilibrium of confined fluid obtained by Sobecki et al. (2019) are then compared to results achieved by several pore radius dependent EOS models in Section 2. Secondly, in the literature, the confinement effect on reservoir production has been mainly studied with a single pore size model in large simulation cells, but the impact of pore size distribution inside a simulation cell, especially in the scale of matrix–fracture transfer, has been poorly considered. In Section 3 of this paper, we therefore present the study of the pore size distribution on the matrix–fracture transfer problem using fine grid simulations. Then in order to perform large scale reservoir simulation, an upscaling methodology of the pore size distribution is investigated on a coarse grid model for matrix–fracture exchange simulations in Section 4. A new triple-porosity model together with a MINC approach is proposed. Finally an application case is presented in Section 5, a large scale reservoir simulation of a stimulated reservoir volume using the developed triple porosity model is presented.

2. Thermodynamic modeling of fluid in nanopores

Different methods to model the thermodynamic behavior of confined fluid using EOS have been developed in the literature as explained in the introduction. In the following subsections, the approaches used in this work, i.e. flash with capillary pressure and flash with critical point shift are presented in details. The different equations and the steps of the algorithms will be clearly described. Then a comparison with reference molecular simulation results from Sobecki et al. (2019) are presented in order to highlight the best flash algorithm method to model thermodynamic of fluid in nanopores.

Table 1
Cubic formulation of EOS for mixture.

	A_m	B_m	$(a\alpha)_m$	b_m
Liquid	$\frac{(a\alpha)_m p^l}{R^2 T^2}$	$\frac{b_m p^l}{RT}$	$\sum_i \sum_j x_i x_j \sqrt{a_i a_j \alpha_i \alpha_j}(1 - k_{ij})$	$\sum_i x_i b_i$
Vapor	$\frac{(a\alpha)_m p^v}{R^2 T^2}$	$\frac{b_m p^v}{RT}$	$\sum_i \sum_j y_i y_j \sqrt{a_i a_j \alpha_i \alpha_j}(1 - k_{ij})$	$\sum_i y_i b_i$

Table 2
Peng–Robinson EOS parameters for mixture.

a_i	b_i	α_i	T_{ri}
$\Omega_a \frac{R^2 T_{ci}^2}{P_{ci}}$	$\Omega_b \frac{RT_{ci}}{P_{ci}}$	$(1 + m_i(1 - \sqrt{T_{ri}}))^2$	$\frac{T}{T_{ci}}$

2.1. Flash with capillary pressure

As explained in the introduction, a lot of authors have included capillary pressure in the flash calculation in order to model the thermodynamic behavior of a confined fluid (Alharthy et al., 2013; Firincioglu et al., 2012; Haider and Aziz, 2017; Rezaveisi et al., 2015; Sandoval et al., 2016; Stimpson and Barrufet, 2016; Teklu et al., 2014; Xiong et al., 2015; Zhang et al., 2016a). Based on the different approaches used by the authors, a flash algorithm is proposed in this section with some improvement according to the convergence issues. The different steps and equations will be detailed.

In a confined fluid, liquid and vapor pressure are no longer considered equal. Their difference is represented by the capillary pressure, which is modeled by the Young–Laplace equation.

$$p_c = p^v - p^l = \frac{2\sigma_{vl} cos\theta}{r} \tag{1}$$

with p^v: vapor pressure, p^l: liquid pressure, σ_{vl}: interfacial tension (IFT) θ: contact angle between the surface of the wetting phase and the wall of the tube r: capillary radius

The IFT is calculated by an analytical Parachor model proposed by Zuo and Stenby (1998):

$$\sigma_{vl} = (P_l \rho^l - P_v \rho^v)^\nu \tag{2}$$

$$P_l = \sum x_i P_i \tag{3}$$

$$P_v = \sum y_i P_i \tag{4}$$

$$P_i = (8.21307 + 1.97473\omega_i) T_{ci}^{1.03406} P_{ci}^{-0.82636} \tag{5}$$

with $\nu = 3.6$, σ_{vl}: interfacial tension (dynes/cm = mN/m), P_l: liquid parachor, P_v: vapor parachor, ρ^l: molar density of liquid phase (mole/cc), ρ^v: molar density of vapor phase (mole/cc), ω_i: acentric factor of component i, T_{ci}: critical temperature of component i (K), P_{ci}: critical pressure of component i (bar).

The cubic Peng and Robinson (1976) EOS function of compressibility factor Z Eq. (6) is used to model the confined fluid in liquid and vapor phase. A_m and B_m are expressed in Table 1.

$$Z^3 + (B_m - 1)Z^2 + (A_m - 3B_m^2 - 2B_m)Z - (A_m B_m - B_m^2 - B_m^3) = 0 \tag{6}$$

where:

$$\alpha(T) = (1 + m(1 - \sqrt{T_r}))^2$$
$$T_r = \frac{T}{T_c} \tag{7}$$

k_{ij} is an empirically determined correction factor which is called the binary interaction coefficient. These coefficients are used to model the intermolar interactions through empirical adjustment of the $(a\alpha)_m$. a_i, α_i and b_i are function of critical temperature T_{ci} and pressure P_{ci}, acentric factor ω_i, liquid molar fraction x_i and vapor molar fraction y_i of each component i of the mixtures as detailed in Table 2 and Eq. (8).

$$m_i = 0.3796 + 1.54226\omega_i - 0.2699\omega_i^2, \ if \ \omega_i \leq 0.49$$
$$m_i = 0.379642 + 1.48503\omega_i - 0.1644\omega_i^2 + 0.016667\omega_i^3, \tag{8}$$
$$if \ \omega_i > 0.49$$

with $\Omega_a = 0.45724$, $\Omega_b = 0.0778$, R: ideal gas constant.

The fugacity coefficient of component i in a mixture is defined for liquid Eq. (9) and vapor Eq. (10) as:

$$\Phi_i^l = \frac{f_i^l}{x_i p^l} \tag{9}$$

$$\Phi_i^v = \frac{f_i^v}{y_i p^v} \tag{10}$$

with f_i^v: fugacity of component i in the vapor phase, f_i^l: fugacity of component i in the liquid phase.

At equilibrium ($f_i^v = f_i^l$), the ratio, $K_i = \frac{y_i}{x_i}$, can be redefined in terms of fugacity coefficient and capillary pressure Eq. (11) (Shapiro and Stenby, 2001).

$$K_i = \frac{y_i}{x_i} = \frac{f_i^v / (\Phi_i^v p^v)}{f_i^l / (\Phi_i^l p^l)} = \frac{p^l \Phi_i^L}{p^v \Phi_i^v} = \left(\frac{p^l}{p_c + p^l} \right) \frac{\Phi_i^l}{\Phi_i^v} \tag{11}$$

The proposed flash algorithm is illustrated in Fig. 1. The initial condition are the same as for the flash without confinement. In addition, we need to set a pore radius r, a contact angle θ and the reference pressure. In this work the contact angle θ is considered to be zero for all the simulations, and the reference pressure is considered to be the pressure of the liquid as mass conservation equation resolution in compositional reservoir simulators is generally performed for oil. The different steps are detailed below.

- Step 1: The initial value of K_i is computed by the Wilson's equation (12) for each components i and capillary pressure is considered to be zero initially.

$$K_i^A = \frac{P_{ci}}{p} exp \left(5.37(1 + \omega_i) \left(1 - \frac{T_{ci}}{T} \right) \right) \tag{12}$$

- Step 2: The Rachford–Rice equation (Eq. (34)) is solved to determine the vapor molar fraction V. This equation is solved by a combination of the Newton–Raphson and binary search method. If the solution does not convergence after 20 Newton–Raphson iterations, the binary search method is applied. The procedure adopted is the negative flash developed by Whitson and Michelsen (1989). Then unphysical values of molar fraction (V or L higher than 1 or lower than 0) are considered as they still give physical values for x_i and y_i. The solution V is between $V_{min} = \frac{1}{1 - max(K_i)}$ and $V_{max} = \frac{1}{1 - min(K_i)}$ which represent the limits of the binary search method. The solution V gives $L = 1 - V$, $x_i = \frac{z_i}{L + V K_i}$ and $y_i = \frac{z_i K_i}{L + V K_i}$.
- Step3: The cubic Peng–Robinson EOS (Eq. (6)) is solved for liquid and vapor phases to get Z^l and Z^v. Then the fugacity coefficients Φ_i^l and Φ_i^v are determined using the equations of fugacity coefficient (Eqs. (31) and (32)).
- Step 4: The interfacial tension is calculated by the parachor model of Zuo and Stenby (1998) (Eq. (2)). Then capillary pressure p_c is calculated by the Young–Laplace equation (Eq. (1)).
- Step 5: The new equilibrium ratio K_i is calculated as a function of capillary pressure (Eq. (11))
- Step 6: The convergence of fugacity and capillary pressure is checked. If the convergence is achieved, then the solution has been reached. If not, steps 2 to 5 are repeated with the new K_i value. The update of the capillary pressure in the loop follows an under-relaxation scheme in order to avoid convergence issues, especially during reservoir simulations. Indeed the Rachford–Rice equation has a physical solution only if one of the K_i is

higher than one (Whitson and Michelsen, 1989). Considering the formulation of the update of K_i (Eq. (11)), the value of the capillary pressure cannot be too high in an iteration step for the flash calculation. In our algorithm, the capillary pressure is increased gradually by a factor of $\frac{1}{\alpha}$ in the iterations. The value of α generally used is 10.

2.2. Flash with critical point shift

As explained in the introduction, the flash with shift of critical point is the second main method used in the literature (Devegowda et al., 2012; Alharthy et al., 2013; Jin et al., 2013; Sanaei et al., 2014; Teklu et al., 2014; Dong et al., 2016a; Haider and Aziz, 2017). This method does not need a modification of the standard flash. Only the input parameters such as critical temperature T_{ci} and critical pressure P_{ci} have to be modified for each components i and a given pore size. The challenge is to get accurate correlations of the evolution of critical properties versus pore size. Thanks to the molecular simulation study performed by Sobecki et al. (2019), two correlations, one for critical temperature and one for critical pressure have been validated using molecular simulation results as reference. The correlation of Jin et al. (2013) Eq. (37) is used for critical temperature and the one from Meyra et al. (2005) Eq. (35) is used for critical pressure evolution versus pore size. These correlations have been validated for pure components. It is considered that these correlations are still valid for a lumped fluid. Furthermore, they are extensible for mixture, i.e. they can model the critical point of the mixtures numerically by the mean of the EOS (Sobecki et al., 2019). It is important to mention that this method is not rigorous from the physical sense. The critical pressure and temperature are intrinsic properties of molecules. Their modification alters the fluid and modify transport and volumetric properties in the single phase. This method could be improved by considering a change of the acentric factor of each molecules.

The two methods of flash with capillary pressure and shift with critical point can also be used together. In that case the correlations are used to calculate critical pressure and temperature for a specific pore size, then these input values are used in the flash with capillary pressure detailed in Section 2.1.

2.3. Comparison to molecular simulation results

The thermodynamic properties at liquid/vapor equilibrium of confined hydrocarbon mixtures obtained using molecular simulation (Sobecki et al., 2019) are considered as reference data for the evaluation of the different EOS modification presented in Sections 2.1 and 2.2. The effect of confinement on fluid properties can be observed in Figs. 2 and 3. The bulk results are represented in black crosses (Gibbs Ensemble Monte Carlo (GEMC) NPT molecular simulation) and the confined fluid results are represented in red circles (confined GEMC NVT molecular simulation). The details about the GEMC simulation in the isotherm–isobar ensemble (NPT) and the canonical ensemble (NVT) are given in Sobecki et al. (2019). The vapor density increases and the liquid density decreases with confinement (Figs. 2 and 3 right). The critical pressure decreases with a value below the bulk value and the bubble point decreases whereas the dew point increases with confinement (Figs. 2 and 3 left). The three main methods used in the literature such as flash with capillary pressure, flash with shift of critical point and flash with both methods used together have been compared with molecular simulation results for methane/ethane in a 3 nm slit pore at 240 K (Fig. 2) and for ethane/n-pentane in a 3 nm slit pore at 370 K (Fig. 3).

The Peng–Robinson EOS (black curves) match very well the molecular simulation results for a bulk fluid. The objective here is to find a good modified EOS which has the best possible match with confined molecular results. For the flash simulations with capillary pressure, gas pressure is used as reference in the algorithm (Fig. 1) instead of

oil because the mixtures are mainly composed of light components. In comparison with the results for a bulk fluid (black curves), the results using the flash with capillary pressure method (blue curves) show a lower bubble point and dew point. The phase envelope is like rotating around the bulk critical point. The critical point is constant with confinement because the fluid is monophasic in that state and then capillary pressure is equal to zero. Vapor density is almost the same than the bulk fluid and liquid density decreases compared to the bulk fluid. The flash with critical point shift (green curves) uses two different correlations for critical temperature and pressure as explained in Section 2.2. The bubble point decreases or increases compared to the bulk fluid according to the mixture composition and the dew point increases. The vapor density increases and the liquid density decreases compared to the bulk fluid. Overall the flash with shift of critical point gives better results than the flash with capillary pressure for these two examples. But the method of flash with capillary pressure and shift of critical properties (purple curve) is the most suitable method for matching the reference molecular simulation data of methane/ethane and ethane/n-pentane in 3 nm slit pore (red circles). For the two mixtures studied, the match is very good for the phase envelope but some improvement must be done for the density. A volume correction such as Péneloux et al. (1982) which is independent of the flash calculation can be used. However, this modification is out of the scope of the present paper.

3. Matrix/fracture interaction with pore size distribution

The flash with capillary pressure presented in Section 2.1 has been included in a reservoir simulator (Wu, 1998; Xiong, 2015). In this Section, the mathematical model of the compositional simulator will be presented for a single porosity model. Then some simulations for different matrix block geometries with different pore size distribution are performed and results are analyzed.

3.1. Mathematical model

The single porosity compositional model is based on the mole conservation equation of every hydrocarbon component i and water.

$$\begin{cases} \frac{\partial M^i}{\partial t} = F^i + q^i \\ \frac{\partial M^w}{\partial t} = F^w + q^w \end{cases} \tag{13}$$

where i represents the hydrocarbon components (total number n_c) and w the water component.

The mass balance equation is evaluated by moles. The accumulation term M^i describes the variation of mole per unit of volume and time. It is equal to the mole flux exchange term F^i plus the internal sink/source term per unit of volume q^i for each component. We consider that there is no mole transfer between hydrocarbon (oil and gas) phases and water phase.

The accumulation term of the hydrocarbon components i and water is expressed by:

$$\begin{cases} M^i = \epsilon(\rho_o S_o x_i + \rho_g S_g y_i) \\ M^w = \epsilon \rho_w S_w \end{cases} \tag{14}$$

with ϵ: the reservoir porosity, ρ_o and ρ_g: the oil and gas molar densities, S_o and S_g: the oil and gas saturations, x_i and y_i: the oil and gas molar fraction of each components. ρ_w: water molar density, S_o: oil saturation.

The mole flux from molecular diffusion is considered negligible. Therefore the mole flux for each hydrocarbon components i and water is calculated from Darcy flow by the following equation:

$$\begin{cases} F^i = -\nabla \cdot (\rho_o x_i \vec{v}_o + \rho_g y_i \vec{v}_g) \\ F^w = -\nabla \cdot (\rho_w \vec{v}_w) \end{cases} \tag{15}$$
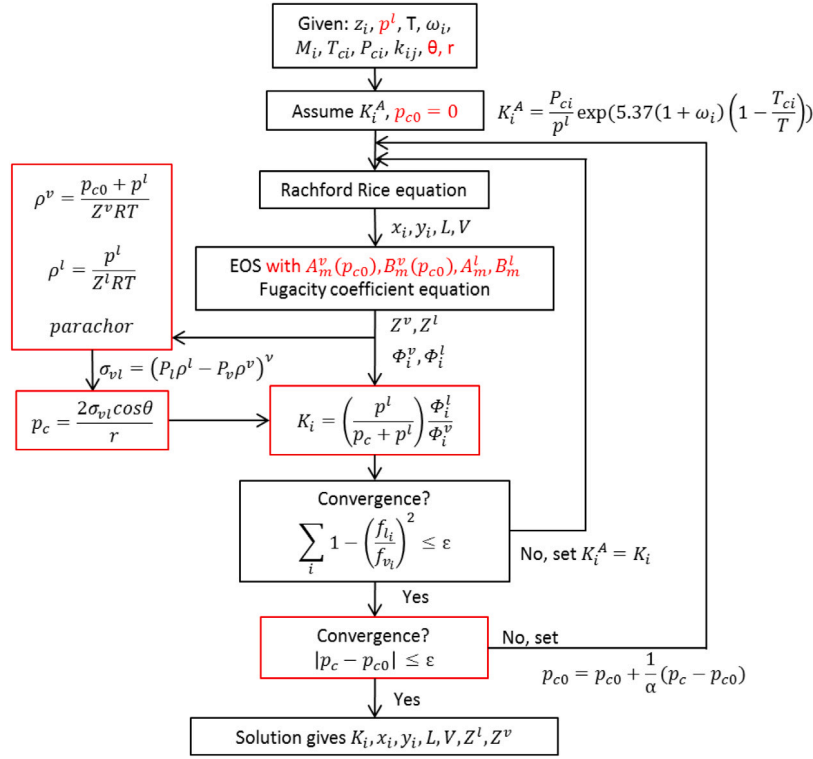
Fig. 1. Algorithm of the flash with capillary pressure. (For interpretation of the references to color in this figure legend, the reader is referred to the web version of this article.)
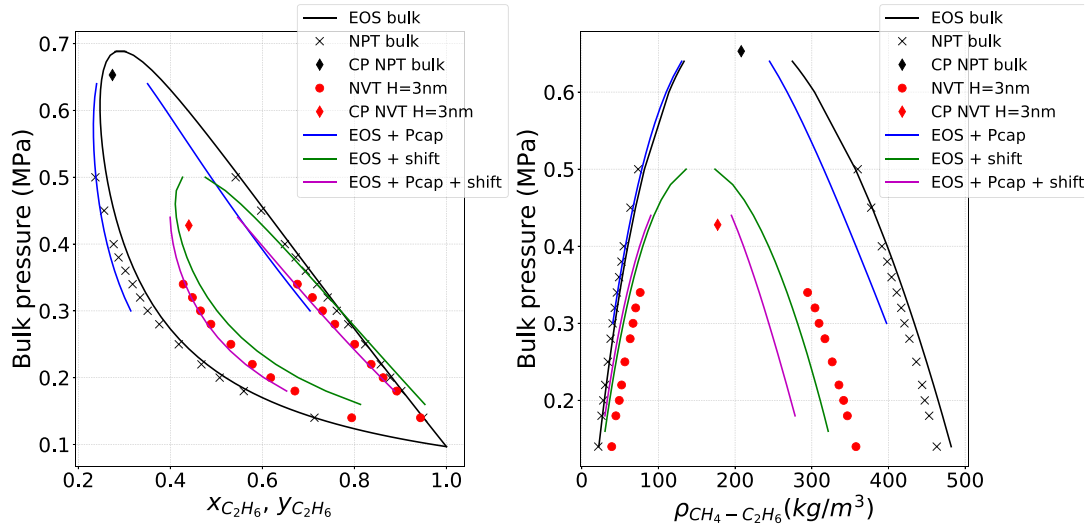

Fig. 2. Comparison of EOS modifications with molecular simulation results for methane/ethane mixture at 240 K in a 3 nm slit pore obtained from Sobecki et al. (2019). The graphs represent pressure versus ethane liquid molar fraction (left) and pressure versus methane/ethane density (right). EOS bulk corresponds to the results obtained from standard EOS. CP corresponds to critical point. NPT bulk and NVT H = 3 nm correspond to the results obtained from molecular simulation for a bulk fluid in the NPT ensemble and a fluid confined in a 3 nm slit pore in the NVT ensemble respectively (see Sobecki et al., 2019). EOS + Pcap corresponds to a flash with capillary pressure with a 3 nm pore length. EOS + shift corresponds to a flash with shift of critical pressure and temperature following the Meyra et al. (2005) and Jin et al. (2013) correlation respectively with a 3 nm pore length. EOS + Pcap + shift corresponds to both methods used at the same time.

$\vec{v}_\phi$ is the Darcy velocity of each phase ϕ = o, g, w: oil, gas and water:

$$\vec{v}_\phi = \frac{kk_{r\phi}}{\mu_\phi}\nabla(p_\phi - \rho_\phi g Z_{res}) \qquad (16)$$

with k: reservoir absolute permeability, $k_{r\phi}$: relative permeability of phase ϕ, μ_ϕ: viscosity of phase ϕ, p_ϕ: pressure of phase ϕ, g: gravity coefficient, Z_{res}: reservoir depth.

The liquid and gas viscosities are calculated using the correlation from Lohrenz et al. (1964). The viscosity of water is considered constant or implemented by a table.

The governing equations of the flow of each fluid component are fully implicitly discretized using finite-volume method and solved by the Newton–Raphson method.
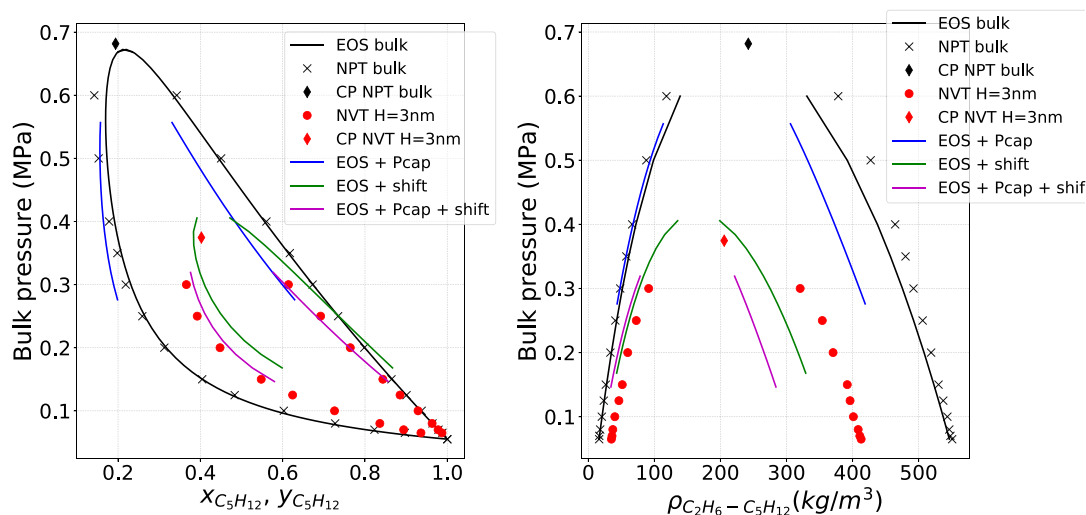
Fig. 3. Comparison of EOS modifications with molecular simulation results for ethane/n-pentane mixture at 370 K in a 3 nm slit pore obtained from Sobecki et al. (2019). The graphs represent pressure versus *n*-pentane liquid molar fraction (left) and pressure versus ethane/*n*-pentane density (right). EOS bulk corresponds to the results obtained from standard EOS. CP corresponds to critical point. NPT bulk and NVT H = 3 nm correspond to the results obtained from molecular simulation for a bulk fluid in the NPT ensemble and a fluid confined in a 3 nm slit pore in the NVT ensemble respectively (see Sobecki et al., 2019). EOS + Pcap corresponds to a flash with capillary pressure with a 3 nm pore length. EOS + shift corresponds to a flash with shift of critical pressure and temperature following the Meyra et al. (2005) and Jin et al. (2013) correlation respectively with a 3 nm pore length. EOS + Pcap + shift corresponds to both methods used at the same time.

Table 3
Compositional data for Bakken oil.

Component	z_i	p_c (MPa)	T_c (K)	M_i (kg/kgmol)	ω_i	V_c (m3/kgmol)
C1	0.36736	4.599	190.56	16.04	0.0115	0.0986
C2	0.14885	4.872	305.32	30.07	0.0995	0.1455
C3	0.09334	4.248	369.83	44.10	0.1523	0.2000
C4	0.05751	3.796	425.12	58.12	0.2002	0.2550
C5–C6	0.06406	3.181	486.38	78.30	0.2684	0.3365
C7–C12	0.15854	2.505	585.14	120.56	0.4291	0.5500
C13–C21	0.0733	1.721	740.05	220.72	0.7203	0.9483
C22–C80	0.03707	1.311	1024.72	443.52	1.0159	2.2474

Table 4
Binary interaction parameters for Bakken oil.

	C1	C2	C3	C4	C5–C6	C7–C12	C13–C21	C22–C80
C1	0	0.005	0.0035	0.0035	0.0037	0.0033	0.0033	0.0033
C2	0.005	0	0.0031	0.0031	0.0031	0.0026	0.0026	0.0026
C3	0.0035	0.0031	0	0	0	0	0	0
C4	0.0035	0.0031	0	0	0	0	0	0
C5–C6	0.0037	0.0031	0	0	0	0	0	0
C7–C12	0.0033	0.0026	0	0	0	0	0	0
C13–C21	0.0033	0.0026	0	0	0	0	0	0
C22–C80	0.0033	0.0026	0	0	0	0	0	0

Table 5
Simulation parameters.

	Matrix	Fracture
k(D)	10^{-7}	10
porosity	facies dependent	1
Initial pressure (bar)	200	
Initial temperature (K)	373.15	
Initial water saturation Swi	0.3	
Fracture pressure (bar)	100	

3.2. Simulation setup

As shale gas and tight oil reservoirs are usually fractured, and the nanopore physics impact only the fluid flows inside the matrix medium and between the matrix and fracture transfer, we will study the matrix–fracture exchange process in the scale of a matrix block size. The pore size distribution (PSD) should be considered in this matrix–fracture interaction where the fracture are explicitly discretized.

In order to study the impact of the PSD on reservoir production, a synthetic reservoir case representing the matrix/fracture interaction has been built with different PSD. The synthetic case is a two dimensional single porosity model representing the matrix/fracture exchange. Pressure in the fracture is maintained at a constant value of 100 bar and only oil and water are present at the initial condition. The initial pressure is 200 bar in the matrix block and depletion is simulated to model flow from the matrix towards the fracture. Bakken oil (Nojabaei et al., 2013; Xiong et al., 2015) is used for the simulations and the different compositional parameters are given in Tables 3 and 4. For information, bubble point of the bulk fluid at the reservoir temperature of 373.15 K is 176.7 bar. All the simulation parameters are summarized in Table 5. The permeability of the matrix has been chosen to be 100 nD in accordance with works from Wang and Reed (2009).

The matrix PSD is divided into three facies corresponding to different ranges of pore size and porosities (Table 6). Facies 1 corresponds to the small pores with pore radius ranging from 2 to 10 nm, Facies 2 corresponds to pores from 10 to 100 nm and Facies 3 corresponds to pore radius above 100 nm, where confinement has no effect on the fluid

phase behavior which is therefore considered as a bulk fluid. The PSD in Facies 1 and 2 is generated by a lognormal distribution with a mean of 3 and a standard deviation of 1 (Fig. 4). Five PSD are considered in the matrix, which correspond to different fractions of the three facies (Table 7). The Table 7 gives the geometric volume fraction v_{fi} of each Facies i and the pore volume fraction $v_{pfi} = \frac{v_{fi}\epsilon_{fi}}{\sum_i v_{fi}\epsilon_{fi}}$ of each Facies i. The distribution D2 corresponds to the PSD of a typical shale reservoir studied by Kuila and Prasad (2013) and interpreted by Alharthy et al. (2013). Five realizations d1, d2, d3, d4, d5 for each of the five PSD: D1, D2, D3, D4 and D5 are generated. Then, in total, twenty five realizations are obtained. A pore radius of 100 nm corresponds to a bulk fluid without confinement effect. It is assumed that the three facies have the same relative permeability but different capillary pressures (Fig. 5). Capillary pressure is assigned according to the pore size, the Facies 3 which corresponds to bulk fluid has zero capillary pressure unlike Facies 1 and 2 (Fig. 5).

The two commonly used methods of flash with capillary pressure (Section 2.1) and flash with critical properties shift (Section 2.2) have
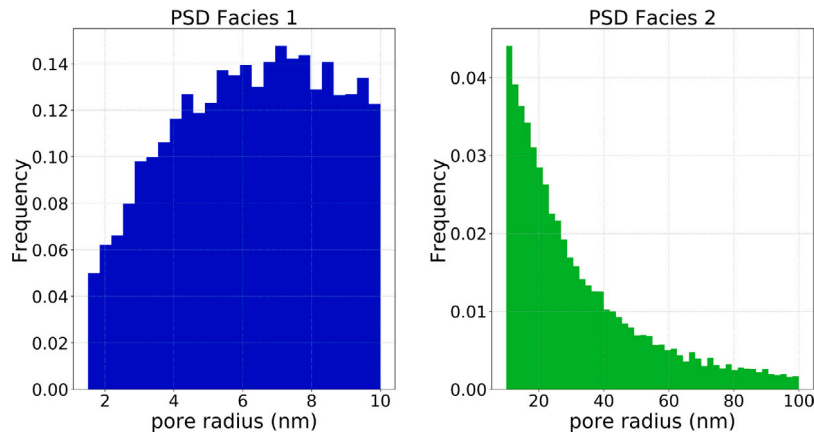
Fig. 4. Histogram of an example of a PSD sample for Facies 1 (left) and 2 (right) using the log-normal law distribution with a mean of 3 nm and a standard deviation of 1 nm.
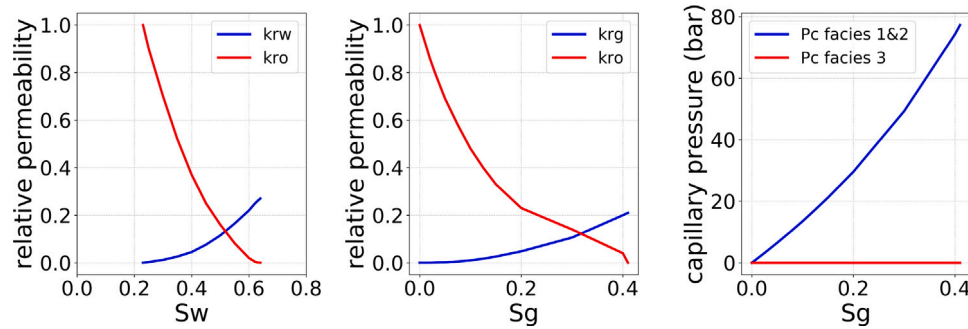

Fig. 5. Oil/water relative permeability (left), oil/gas relative permeability (center) and capillary pressure curves (right).

Table 6
Pore size distribution properties.

Facies	Pore size (nm)	porosity
1	2–10	$\epsilon_{f1} = 0.02$
2	10–100	$\epsilon_{f2} = 0.05$
3	>100	$\epsilon_{f3} = 0.1$

Table 7
Grid volume and pore volume per facies for the different distributions 'D'.

Distribution	Geometric volume fraction (%)			Pore volume fraction (%)		
	Facies 1 (v_{f1})	Facies 2 (v_{f2})	Facies 3 (v_{f3})	Facies 1 (v_{pf1})	Facies 2 (v_{pf2})	Facies 3 (v_{pf3})
D1	10	20	70	2.5	12	85.5
D2	19	22	59	5	15	80
D3	20	40	40	6	31	63
D4	25	45	30	9	39	52
D5	35	50	15	15	53	32

Fig. 6. Simulation geometry for the matrix/fracture interaction. Matrix is represented in yellow and fractures are represented in purple around the matrix.

Table 8
Geometry parameters (block size 20 × 20 m).

	Matrix	Fracture
Number of cells	100 × 100 × 1	404
dx/dy/dz (m)	0.2/0.2/0.2	0.001/0.2/0.2 or 0.2/0.001/0.2

been chosen for the PVT modeling of the fluid in Facies 1 and 2. The fluid in Facies 3 is considered to have no confinement effect, then the flash is not modified.

3.3. Simulation of matrix/fracture transfer with fine grid

A tight matrix rock of 20 m length, 20 m width and 0.2 m thickness (in yellow Fig. 6) is surrounded by a fracture of 0.001 m width (in purple Fig. 6). In order to get reliable results, the grid is very fine with grid cells of 0.2x0.2x0.2 m. The parameters of the geometry are summarized in Table 8.

An example of one of the five realizations d1 for distribution D2 is showed in Fig. 7. The left part of the figure corresponds to one of the five realizations of the spacial distribution of the three facies: 1, 2, 3
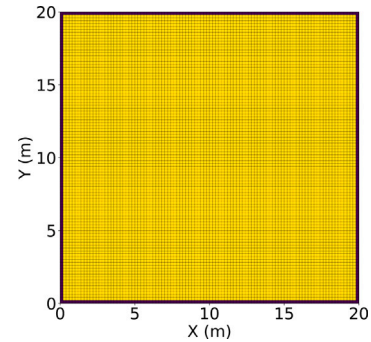
for D2. The Facies 0 corresponds to the fracture. The right part of the figure corresponds to the pore size values in these three facies.

Before showing production results for different pore size distributions detailed in the previous section, results of recovery factor and GOR for homogeneous pore size inside the matrix are presented in Fig. 8 for the same simulation setup. This is currently the commonly used method in the literature for considering PSD (Firincioglu et al., 2013; Sanaei et al., 2014; Alharthy et al., 2017; Haider and Aziz, 2017; Lopez Jimenez et al., 2018). The simulation for the bulk fluid has no
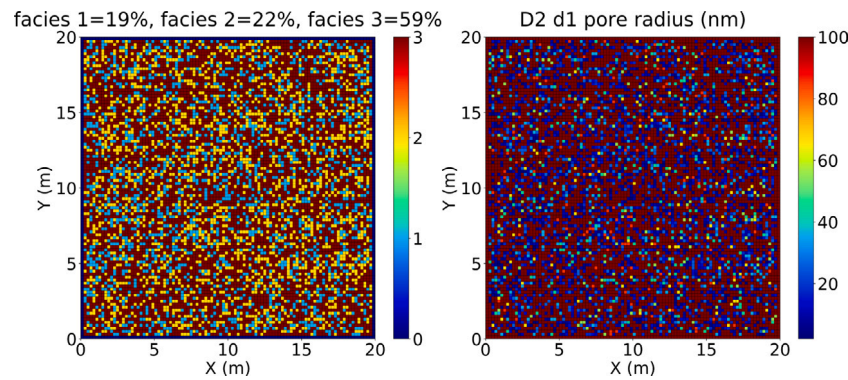
Fig. 7. Example of facies (left) and pore size distribution (right) for D2.

capillary pressure and no modification of the flash. The simulations for homogeneous pore size inside the matrix have no capillary pressure for fluid flow and a modified flash with capillary pressure (Section 2.1) in the matrix. The confinement reduces the gas–oil ratio (GOR) and keeps it constant for a longer time, which is consistent with observations on the field and in the literature (see introduction). As gas apparition is postponed during depletion because of the reduction of bubble point, confinement decreases the gas accumulation. Furthermore, the oil keeps its low density and viscosity for a longer time during depletion because its light components stay in the liquid phase. Then confinement helps to produce more oil but gas apparition also allows to keep the reservoir pressure high. That is why 3 nm and 5 nm confinement cases produce less oil than the bulk case.

Considering a single average radius inside the matrix for a PSD in the scale of a matrix block has been used by many authors in the literature (Firincioglu et al., 2013; Sanaei et al., 2014; Alharthy et al., 2017; Haider and Aziz, 2017; Lopez Jimenez et al., 2018). But this approach is not accurate as heterogeneity of capillary pressure and pore size dependent PVT behavior is not taken into account. That is why in this work, the PSD is explicitly described with one pore radius in each cells at very fine scale. As explained in the previous section, five simulations corresponding to different realizations have been performed for each distribution D. Fig. 27 in Appendix A.2 is an example of the production results for the five realizations of D1. Although spacial heterogeneity of PSD, capillary pressure and PVT behavior are different due to extremely small pore sizes, the results are quite similar for each of the five realizations 'd'. This is because the pore size realization is not spatially correlated and this kind of distributions can be homogenized in the considered volume, which is a representative element volume. In order to compare the different distributions 'D', the production data of the five realizations of each 'D' is represented by their average value P50 (percentile 50). We first present the results with flash with capillary pressure used for PVT modeling for Facies 1 and 2.

The gas and oil recovery factors and the gas–oil ratio (GOR) of the different distributions D are compared to the same case simulations using a bulk fluid in Fig. 9. The bulk fluid is represented with zero capillary pressure in the entire matrix and no modification of the flash. As the porosities are different for each distributions D, the simulation production results for a bulk fluid are also different. For all cases, the oil production increases, the gas production and the GOR decreases with fluid confinement in comparison with the bulk fluid results. Two different effects are present and can explain this observation: the capillary pressure heterogeneity and the pore size dependent PVT modeling of the fluid. The capillary pressure heterogeneity slows down or even stop the gas flow from Facies 3 to fractures. The Facies 3 gathers the most of the fluid because it represents the largest volume of the matrix. In its flow from matrix to fracture, the gas mainly present in Facies 3 will flow through Facies 2 and Facies 1 where the capillary pressure is very high. As there is no capillary pressure in Facies 3, a large volume

of gas stays stuck in Facies 3. The matrix pressure will then be maintained for a longer time. Therefore gas production decreases and oil production increases, then the GOR does not increase. The results are consistent with field observations of constant production GOR during depletion (Khoshghadam et al., 2017; Kumar, 2007; Nojabaei et al., 2013; Tian et al., 2013). On the other hand the modification of the flash with capillary pressure decreases the bubble point of the oil. Gas apparition is then postponed during depletion and oil stays lighter for a longer time, which leads to the same conclusion for production results: decrease of gas production, increase of oil production and constant GOR which is consistent with field observations (Khoshghadam et al., 2017; Kumar, 2007; Nojabaei et al., 2013; Tian et al., 2013). These two effects of capillary pressure heterogeneity blocking gas volume in large pores and modified PVT behavior effect postponing gas apparition can be seen in Fig. 10. Indeed we can see an heterogeneity of the gas pressure field and the gas saturation field from the center of the matrix to the fracture. Given areas have high gas pressure and saturation.

Lets focus now on the comparison of the P50 value of reservoir production for the different distributions D (Fig. 9). When the volume fraction of nanopores of Facies 1 and 2 increases (i.e. from D1 to D5), the production of oil increases until D4 and then decreases. Furthermore the gas production and the GOR decreases until D3 or D4 (they have almost the same P50) and then increases. The capillary pressure heterogeneity has a strong impact on production for low percentage of nanopores in the matrix because large volume of Facies 3 might be surrounded by Facies 1 and 2 where the capillary pressure is very high. Then important volume of gas stays stuck in Facies 3. When the percentage of nanopores becomes important (D4, D5), the volume of Facies 3 surrounded by Facies 1 and 2 is very small and no gas entrapment occurs. However the volume of cells with lower bubble point due to modified PVT modeling becomes significant to impact the production. For the studied cases it seems that the impact on production of capillary pressure heterogeneity is more important than confined fluid PVT behavior. This could explain the trend inversion of the curves from D4 to D5 seen in Fig. 9.

The impact of pore size dependent PVT modeling can be analyzed by comparing reservoir simulation models with capillary pressure heterogeneity with and without confined fluid PVT model. A simulation without confined fluid PVT model corresponds to a classic flash for a bulk fluid. Fig. 11 shows the difference between these two models for d1, one of the five realizations. The two different models are quite similar from D1 to D3 which mean that modified PVT modeling has no strong impact on production for such distributions. However for D4 and especially D5 with higher volume fraction of nanopores in the matrix, the difference between the two models is significant. This means that pore radius dependent EOS has an important impact on production for these distributions with high volume fraction of nanopores.

The production results for the five different distributions 'D' are now presented with flash with shifted critical pressure and temperature (see details in Section 2.2) used for the PVT modeling of Facies 1 and
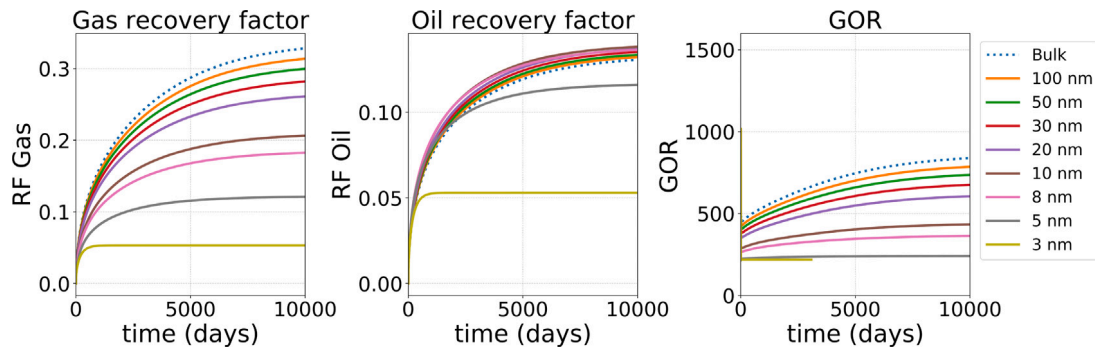
Fig. 8. Production results for homogeneous pore size. The graphs represent gas recovery factor versus time (left), oil recovery factor versus time (center) and gas–oil ratio versus time (right).
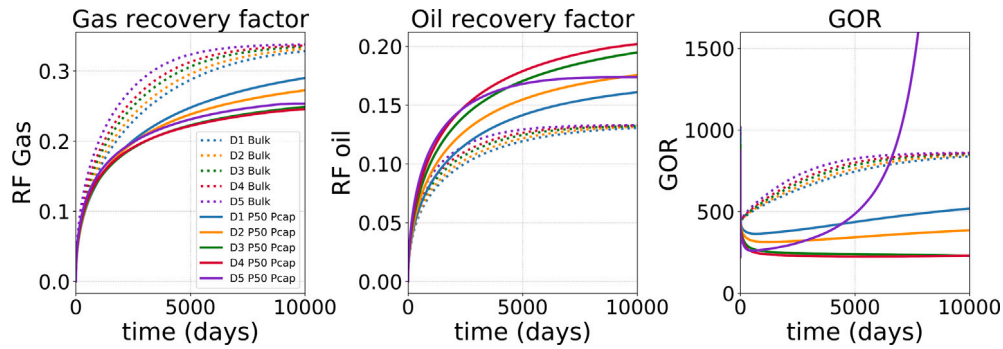

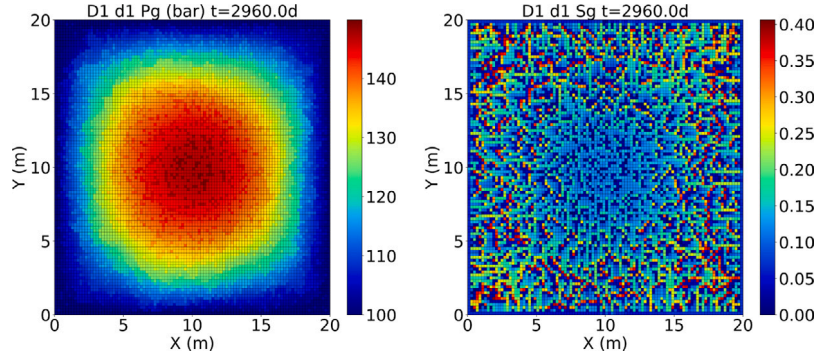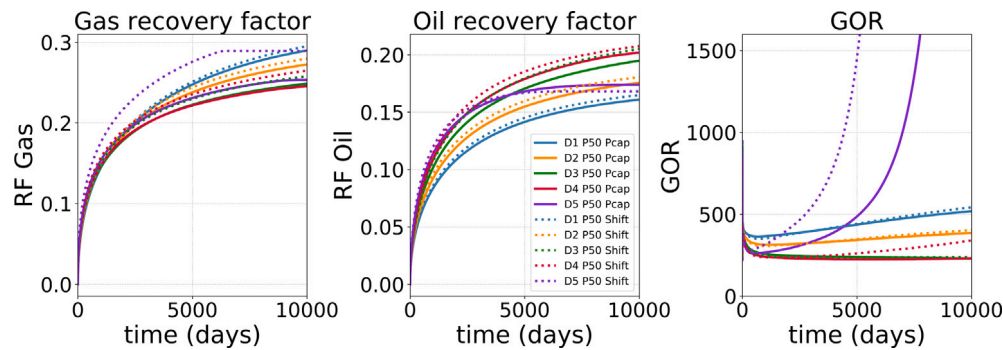**Fig. 9.** Comparison of production results for the different distributions D for bulk and confined fluid with a flash with capillary pressure (P50 Pcap). The graphs represent gas recovery factor versus time (left), oil recovery factor versus time (center) and gas–oil ratio versus time (right).

Fig. 10. Example of gas pressure field (left) and gas saturation field (right) for distribution D1 d1 at 2960 days.
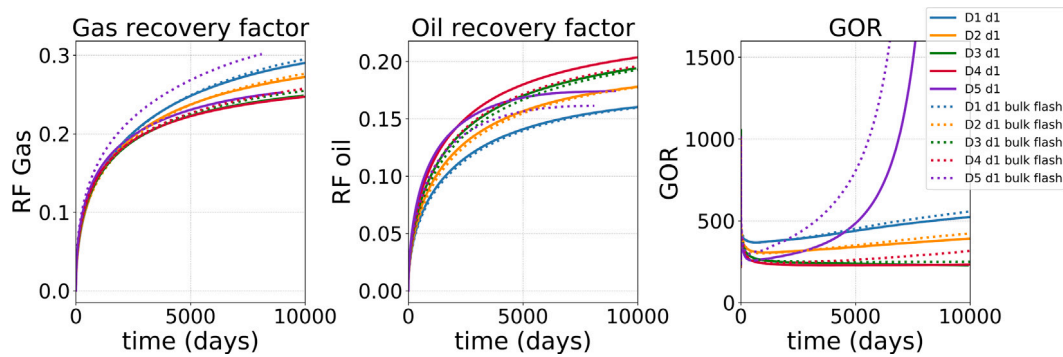
Fig. 11. Impact of modified EOS on production. The full lines correspond to simulation results for a case with capillary pressure heterogeneity in the matrix and flash with capillary pressure for the different distribution D. The dotted lines correspond to simulation results for a case with capillary pressure heterogeneity in the matrix and a standard flash without confinement effect for different distribution D. The graphs represent gas recovery factor versus time (left), oil recovery factor versus time (center) and gas–oil ratio versus time (right).

Fig. 12. Comparison of production results for different distributions 'D' between flash with capillary pressure (Pcap) and flash with critical point shift (Shift). The graphs represent gas recovery factor versus time (left), oil recovery factor versus time (center) and gas–oil ratio versus time (right).

Table 9
Geometry parameters (block size 40 × 10 m).

	Matrix	Fracture
Number of cells	400 × 100 × 1	1004
dx/dy/dz (m)	0.1/0.1/0.1	0.001/0.1/0.1
		or 0.1/0.001/0.1

2 (Fig. 28 in Appendix A.2). The conclusions are similar to the case with a flash with capillary pressure. Compared to the flash with bulk fluid, the oil production increases, the gas production and the GOR decreases with fluid confinement. However it is important to note that changing critical pressure and temperature alters the fluid which provides a different initial mass, transport and volumetric properties in the single phase compared to bulk. Comparing results for a bulk fluid and different distributions 'D' might then not be very proper. That is why we plot and compare the recovery factors. Concerning the evolution of production against the increase nano-pores volume fraction (from D1 to D5), the observations are also the same. The production of oil increases until D4 and then decreases, the production of gas and the GOR decreases until D3 and then increases. The explanations used for the case of flash with capillary pressure are applicable to the case of flash with critical point shift.

The comparison of the production results for the two flash methodologies (flash with capillary pressure and flash with critical point shift) is shown Fig. 12. The results for D1, D2 and D3 are very similar. Indeed the small pores have a low volume fraction inside the matrix, so the impact of modified PVT modeling is negligible compare to capillary pressure heterogeneity. However for D4 and D5 with a higher proportion of nanopores, the difference is quite significant because the two modified PVT models are different.

The same simulations for the five distributions 'D' have been performed for a different matrix/fracture geometry with a matrix block size of 40 × 10 m. The geometry is also made up of a tight matrix surrounded by a fracture. The dimensions and the number of cells are summarized Table 9. All the simulation setups are the same as detailed in Section 3.2. The simulation results of the new matrix block size of 40 × 10 m is presented in Appendix A.2 Fig. 29. The flash with capillary pressure methodology is used. The trend of the production curves for the different distributions are similar to the initial geometry with the matrix block size of 20 × 20 m, but with a different time scale.

The simulations using a flash with capillary pressure and critical point shift have also been performed, but we encountered some convergence issues on this example. Hence, although the flash with both capillary pressure and shift of critical properties has been proven as the best way to model the confined fluid behavior in Section 2, the flash with only capillary pressure will be used for the investigation and development of upscaling methodologies in the next section. The choice of a thermodynamic model has no impact on the validity of the upscaling technique for the triple-porosity model presented hereafter.
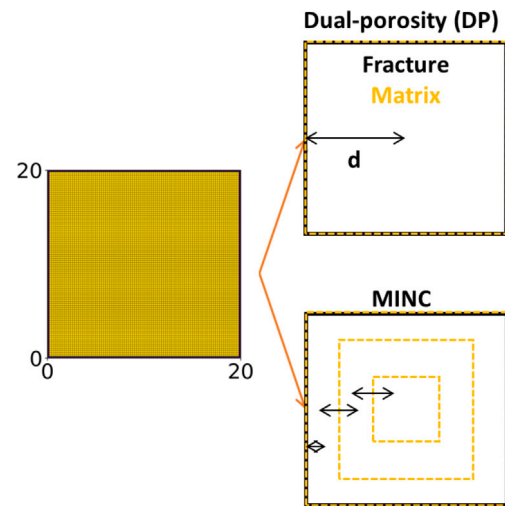

Fig. 13. Dual porosity model with and without MINC matrix discretization.

4. Reservoir simulation in a large scale

The matrix/fracture exchange modeling is crucial for accurate tight oil and shale gas reservoir production forecasting. In order to perform large scale reservoir simulations, large gridblocks are required, and upscaling methodologies must be developed because of computational constraints and very detailed characterization of matrix and fracture spacial distribution and geometries. The upscaling of the matrix/fracture interaction is more complex than that in conventional reservoirs because of low matrix permeability and very heterogeneous PSD with pore radius dependent PVT. Some methodologies are proposed in the literature. The previous study of matrix/fracture interaction at very fine scale in Section 3 gives reference results to investigate upscaling methodologies. The first part 4.1 of this section therefore presents and investigates the different upscaling methodologies proposed in the literature. Then a new triple porosity model is proposed and its mathematical model is detailed in Section 4.2. The upscaling methodology of the triple porosity and its validation by the reference results is presented in Section 4.3.

4.1. Dual porosity and MINC methodologies

The dual-porosity model was originally developed by Barenblatt et al. (1960) and Warren and Root (1963). It represents a fractured reservoir with two media: matrix and fracture. In a grid, any matrix cell is associated to a fracture cell located at the same grid location. Matrix and fracture grids are identical and superposed. In a given cell,

there are N identical matrix block and each one behaves as a block located at the center of the cell.

The MINC model stands for 'Multiple INteracting Continua' and has been developed by Pruess and Karasaki (1982) and Pruess (1985). The MINC model is an extension of the dual porosity model as it divides the matrix block into a series of nested volume on the basis of the distance from the nearest fracture. It allows to take into account the transient state of the flow between matrix and fracture which can be very long for low permeability reservoirs (Wu et al., 2012). MINC method treats the problem entirely by numerical methods in a fully transient way. It consists in a fully transient representation of the inter-porosity flow.

4.1.1. Homogeneous case

The matrix–fracture transfer modeling using dual-porosity model and MINC method is first investigated for an homogeneous case with bulk fluid, ie without pore size dependent PVT model. These methods are illustrated Fig. 13 for the case of the matrix block size of 20×20 m presented in Section 3.2. The production results for a bulk fluid of these two models are compared to the fine grid reference results in Fig. 14. The dual porosity model (D2 2P) is unable to match the fine grid results (Bulk fine). On the contrary the method with ten matrix MINC discretizations (2P MINC 10) matches very well the bulk fine grid results. As the permeability of the matrix is very low, the fracture–matrix interaction shows a long-lasting transient flow (Wu et al., 2012). The quasi-steady state flow assumption of the dual porosity model is therefore unsuitable to model the matrix–fracture interaction. The more rigorous MINC concept is adapted as a generalization of the dual-continuum model. It describes pressure gradient between fractures and matrix by further subdividing individual blocks.

Different shape factor for the dual-porosity simulation have also been tried, and none of them can match the reference solution. The dual porosity model with MINC discretization allows to match the fine grid results of matrix/fracture transfer for a bulk fluid. This model will then be used to investigate the upscaling methodologies of the PSD for a fluid with pore radius dependent PVT.

4.1.2. Heterogeneous case

In the literature two main methods are used for the upscaling of the PSD: the first one considers an average pore radius to account for the PSD and the second one considers a saturation dependent capillary pressure in the flash calculation (Section 2.1). Here, we use these methods to the distribution D2 for the case with matrix block size of 20×20 m (Section 3.2). The flash used for the upscaling methodologies is either a flash with capillary pressure and average radius or a flash with an effective radius function of oil saturation (Fig. 30 in Appendix A.3.1). The production results for a confined fluid in the distribution D2 are given in Fig. 15 for the reference fine grid simulation (D2 P50), for different average radius (D2 DP MINC 10) and the effective radius (D2 DP MINC 10 r_eff).

No average pore radius from 5 nm to 100 nm is able to match the fine grid results. For GOR production the average radius should be between 5 nm and 10 nm. This range of values is impossible to match the reference results for gas and oil production. Therefore upscaling the PSD using an average pore radius seems not to be adapted. The effective radius method gives results very similar to the case of a pore radius of 100 nm. We have seen in Section 3.3 that the confinement effect is negligible for a flash with capillary pressure and pore radius above 100 nm. The results are similar to a flash without confinement modeling a bulk fluid. As the gas saturation in the matrix is low during depletion, the effective radius value is high and a large volume fraction of small pores is neglected. The effective radius method is therefore not adapted to upscale the PSD. None of the upscaling methodologies proposed in the literature are able to match the fine grid production results of a matrix/fracture transfer with a PSD and pore radius dependent PVT. A new triple porosity upscaling methodology is therefore developed in this work.

4.2. New triple porosity model

Multi-porosity models such as triple porosity model have been used in the literature for different applications. There are a lot of studies in hydrology aiming to model the matrix/fracture exchange. Matrix and fractures media are subdivided into several media in order to improve the model accuracy because of the presence of cavities (Liu et al., 2003) or fractures of different scales (Wu et al., 2004). These models have also been used for unconventional reservoir in order to account for the different gas flow regime in function of their Knudsen number and therefore the pore size in the matrix (Wang et al., 2017b,a). Only Alfi et al. (2017) used a triple porosity model to take into account the confined fluid behavior function of pore size and what he called the sieving effect. That method is interesting but seems to have several drawbacks as explained in introduction.

4.2.1. Concept

The idea developed in this work is to conceptualize the matrix/fracture transfer with a PSD into three media: fractures, small pores and large pores. The source of the flow is considered to be mainly in large pores because they gather the largest volume of hydrocarbons. Then in the flow from large pores to fractures, the fluid flows across small pores which surround large pores to finally be produced through the fractures. In other words, the model considers that flow occurs from large pores to fractures through small pores as illustrated in Fig. 16. The direct flow between large pores and fractures is neglected. Peng–Robinson EOS is used in large pores and fractures, and the modified Peng–Robinson with capillary pressure is used in small pores (Section 2.1). The capillary pressure used for flow calculation is equal to zero in large pores and it is function of saturation in small pores. The fluid which is predominantly present in large pores must go through small pores to join the fractures. As the gas–oil capillary pressure of small pore is higher than large pores, the gas flow up to the fracture is slowed down. Furthermore as the PVT model of the small pore is pore size dependent, then the gas apparition is postponed during depletion. Therefore the two effects of capillary pressure heterogeneity and the confined fluid PVT behavior detailed in Section 3.3 are taken into account in the triple porosity model. The three subdomains have their own porosity and permeability respecting the fine grid properties.

4.2.2. Mathematical model

Contrary to the dual-media model, the flow is calculated in three media: large pores, small pores and fracture considering mass transfer between them. The mole conservation equation of every components i for each media: large pores (L), small pores (S) and fractures (F) is expressed by the following equations in moles per unit of volume.

$$\begin{cases} \frac{\partial M_L^i}{\partial t} = F_L^i - F_{LS}^i \\ \frac{\partial M_S^i}{\partial t} = F_S^i + F_{LS}^i - F_{SF}^i \\ \frac{\partial M_F^i}{\partial t} = F_F^i + q_F^i + F_{SF}^i \end{cases} \tag{17}$$

where M_L^i, M_S^i, M_F^i are the accumulation terms of the component i in the media L, S and F respectively. F_L^i, F_S^i, F_F^i are the mole flux exchange of component i in each media. F_{LS}^i is the mole flux between large pores to small pores and F_{SF}^i is the mole flux between small pores to fractures. q_F^i is the internal sink/source term per unit of volume for component i in the fracture. We have similar model for the water component.

The sink/source terms in large pores and small pores are neglected as we consider that the majority of the production/injection occurs in fractures. The large pore medium gives a mole flux F_{LS}^i to the small pore medium. The small pore medium receives mole flux from large pores F_{LS}^i and gives mole flux to fracture F_{SF}^i. Finally the fracture medium received mole flux from small pores F_{SF}^i. The flow model
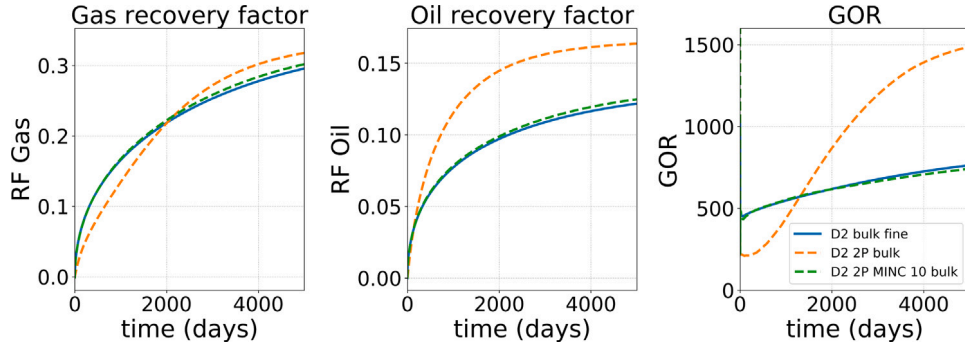
Fig. 14. Production results for a bulk fluid corresponding to distribution D2 using single porosity fine grid model (fine) and standard dual porosity model (2P) and MINC (2P MINC) matrix discretization. The graphs represent gas recovery factor versus time (left), oil recovery factor versus time (center) and gas–oil ratio versus time (right).
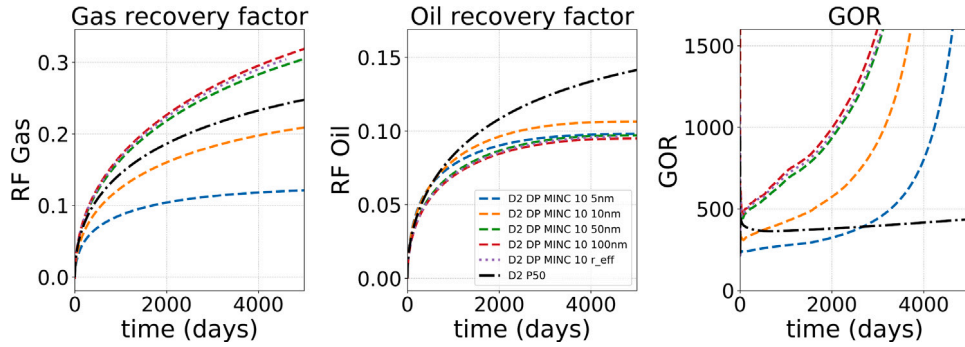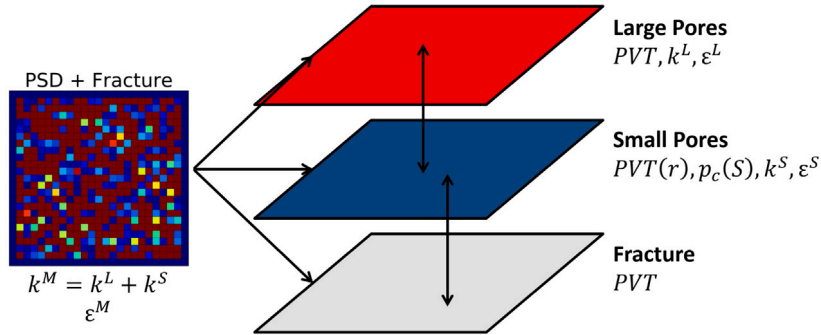

Fig. 15. Production results for distribution D2 using single porosity fine grid model (D2 P50), dual porosity model with MINC matrix discretization (D2 DP MINC 10) and effective radius (D2 DP MINC 10 r_eff). The graphs represent gas recovery factor versus time (left), oil recovery factor versus time (center) and gas–oil ratio versus time (right).

Fig. 16. Schematic of triple porosity model for one matrix/fracture block.

we consider between media explains the additional mole flux terms in Eq. (17).

The accumulation term of the hydrocarbon component i for each medium $\xi = L, S, F$ is expressed by:

$$\begin{cases} M_\xi^i = \epsilon_\xi(\rho_o S_o x_i + \rho_g S_g y_i)_\xi \\ M_\xi^w = \epsilon_\xi(\rho_w S_w)_\xi \end{cases} \tag{18}$$

As in single porosity model, the mole flux for each hydrocarbon component i and water for each medium $\xi = L, S, F$ is calculated from Darcy flow by the following equation:

$$\begin{cases} F_\xi^i = -\nabla \cdot (\rho_o x_i \vec{v}_o + \rho_g y_i \vec{v}_g)_\xi \\ F_\xi^w = -\nabla \cdot (\rho_w \vec{v}_w)_\xi \end{cases} \tag{19}$$

The mole flux terms between media F_{LS}^i and F_{SF}^i are not easy to express analytically. They can be expressed in a discrete form. A finite-volume based method is used for the space discretization of the system of Eq. (17). The mole flux terms per unit of volume F_{LS}^i and F_{SF}^i

can therefore be expressed in their spacial discretization form. Their expression will be detailed in the next section.

4.2.3. Discretization of the model

The main concept and mathematical model of the triple porosity approach have been given in the previous section. The details of the model and the flux term calculation are now presented. The large pore and small pore media are subdivided into several nested meshes using the MINC methodology as illustrated Fig. 17 left for two different reasons. Firstly, the discretization of the matrix allows to take into account the long transient state of the flow between matrix and fracture because of the very low matrix permeability. Secondly, in order to well reflect the flow at fine scale, the triple porosity model also considers internal flow between large and small pores. In the flow from large pore to the fracture, the fluid can flow directly to small pores or continue to flow in another large pore media before finally flow to small pores. In the model, an exchange term is given between the large and small pores for each MINC volume j. The flow between small pores and fractures

is only possible for the out-most small pore MINC volume. This flux is similar to the standard MINC model.

On each MINC volume j, the system of Eqs. (17) can be written in a discretized form in both large and small pore for each component i.

$$\begin{cases} \frac{\partial M_{L,j}^i}{\partial t} = F_{L,j}^i - F_{LS,j}^i \\ \frac{\partial M_{S,j}^i}{\partial t} = F_{S,j}^i + F_{LS,j}^i - F_{SF}^i \end{cases} \tag{20}$$

The flux terms are calculated using their spacial discretization form. Let us take an example of a two dimension rectangular matrix block of dimension $L_{x1} \times L_{y1}$ with isotropic permeability as illustrated Fig. 17. The flux between two MINC volumes j and $j+1$ of a matrix block inside the large pores and small pores medium $\xi = L, S$ for the components i is:

$$\begin{cases} f_{\xi,j,j+1}^i = -\gamma_{j,j+1}^\xi [(\rho_o x_i \lambda_o)_\xi^{j+1} (\Psi_o^{\xi,j} - \Psi_o^{\xi,j+1}) \\ +(\rho_g y_i \lambda_g)_\xi^{j+1} (\Psi_g^{\xi,j} - \Psi_g^{\xi,j+1})] \\ f_{\xi,j,j+1}^w = -\gamma_{j,j+1}^\xi (\rho_w \lambda_w)_\xi^{j+1} (\Psi_w^{\xi,j} - \Psi_w^{\xi,j+1}) \end{cases} \tag{21}$$

$$\gamma_{j,j+1}^\xi = \frac{A_{j,j+1} k^\xi}{d_{j,j+1}} \tag{22}$$

with $A_{j,j+1} = 2(L_{xj} + L_{yj})(dz)$ is the area surrounding a MINC volume j. $\gamma_{j,j+1}^\xi$ the transmissivity between two MINC volumes j and $j+1$ of the medium $\xi = S, L$, ie large pores or small pores. $d_{j,j+1}$ is the distance between two MINC volume j and $j+1$. These parameters are illustrated Fig. 17 right. k^ξ is the permeability of the medium $\xi = S, L$ which is constant for a medium. $\lambda_\phi = \frac{k_{r\phi}}{\mu_\phi}$ is the mobility of phase ϕ. $\Psi_\phi^{\xi,j} = [p_\phi - \rho_\phi g Z_{res}]^{\xi,j}$ is the flow potential of phase ϕ for the MINC volume j of the medium $\xi = S, L$. The terms $(\rho_o x_i \lambda_o)_\xi^{j+1}$, $(\rho_g y_i \lambda_g)_\xi^{j+1}$ and $(\rho_w \lambda_w)_\xi^{j+1}$ are computed with an upstream scheme according to the potential values in large and small pores ($\xi = S, L$).

The flux $F_{\xi,j}^i$ on each MINC volume j of medium $\xi = S, L$ for the component i is defined in the following equation for the two dimensions case. It is similar to the MINC method. The number of matrix blocks inside a cell is equal to $\frac{V_{cell}}{V_{block}}$ with $V_{block} = L_{x1} L_{y1}(dz)$.

$$F_{\xi,j}^i = \frac{V_{cell}}{V_{block}} (f_{\xi,j-1,j}^i + f_{\xi,j,j+1}^i) \tag{23}$$

The flux calculation between large pores and small pore media is a total novelty in this model. It is assumed that the transfer is proportional to an intrinsic parameter α, representing the average pore structure between large and small pores. Moreover, it is proportional to the average surface area perpendicular to the flow direction and inversely proportional to the average traveled distance along the flow direction in the MINC volume. On a MINC volume j the flux is computed by:

$$\begin{cases} F_{LS,j}^i = -\frac{V_{cell}}{V_{block}} \gamma_j^{LS} [(\rho_o x_i \lambda_o)_{\xi,j} (\Psi_o^{S,j} - \Psi_o^{L,j}) \\ +(\rho_g y_i \lambda_g)_{\xi,j} (\Psi_g^{S,j} - \Psi_g^{L,j})] \\ F_{LS,j}^w = -\frac{V_{cell}}{V_{block}} \gamma_j^{LS} (\rho_w \lambda_w)_{\xi,j} (\Psi_p^{S,j} - \Psi_p^{L,j}) \end{cases} \tag{24}$$

$$\gamma_j^{LS} = \alpha \frac{\tilde{A}_j k^M}{\tilde{d}_j} \tag{25}$$

with γ_j^{LS} the transmissivity between the two media large pores and small pores for a MINC volume j. k^M is the permeability in the matrix. $\tilde{A}_j = \frac{2(L_{xj}+L_{yj})+2(L_{xj+1}+L_{yj+1})}{2}(dz)$. $\tilde{d}_j$ is the width of MINC volume j. These parameters are illustrated Fig. 17 right. The average pore structure parameter α depends on PSD and is to be determined. $\xi = S$ or L according to the potential values in large and small pores (upstream scheme).

The flux between the small pore medium nearest MINC volume from the fracture and the fracture medium for components i is approximated by:

$$\begin{cases} F_{SF}^i = -\frac{V_{cell}}{V_{block}} \gamma^{SF} [(\rho_o x_i \lambda_o)_{\xi,1} (\Psi_o^F - \Psi_o^{S,1}) \\ +(\rho_g y_i \lambda_g)_{\xi,1} (\Psi_g^F - \Psi_g^{S,1})] \\ F_{SF}^w = -\frac{V_{cell}}{V_{block}} \gamma^{SF} (\rho_w \lambda_w)_{\xi,1} (\Psi_p^{F,j} - \Psi_p^{S,1}) \end{cases} \tag{26}$$

$$\gamma^{SF} = \frac{A_{0,1} k^{SF}}{d_{0,1}} \tag{27}$$

with γ^{SF} the transmissivity between the outermost MINC volume in the small pore medium and the fracture medium. $A_{0,1} = 2(L_{xj} + L_{yj})(dz)$. The index j = 0 corresponds to the fracture and the index $j = 1$ corresponds to the nearest MINC volume from the fracture. These parameters are illustrated Fig. 17 right. k^{SF} is the average permeability between the nearest MINC volume of small pores from the fracture and the fracture medium. $\xi = S$ or F according to the potentials (upstream scheme).

It is important to only consider the small pore/fracture flow through the nearest MINC subdivision from the fracture. At fine scale only a small volume fraction of the matrix is in contact with the fracture. A small volume fraction of large pores or small pores must therefore be in contact with the fracture. The contact between large pores and fracture is not considered in this model. Indeed considering the flow from large pores to fracture through small pores enables to model the stall phenomenon observed at fine scale because of high capillary pressure in small pores. Therefore only a small volume fraction of small pores is considered in contact with the fracture. This small fraction is modeled by the outermost MINC volume of small pore medium.

The triple porosity model presented in this section has several unknown parameters to be determined. These parameters are the pore structure parameter α which involves in the transmissivity between the large pore and small pore media, the average pore radius value used for the flash in the small pore medium, the permeabilities and the porosities of small pore or large pore medium. They can be matched using the fine grid results as reference. The strategy developed in this work is to use the fine grid results to calibrate the triple porosity model.

4.3. Upscaling

4.3.1. Methodology

The triple-porosity coarse grid simulation is performed on the same matrix block as the fine grid simulation presented in Section 3.2. An initial pressure is given at the matrix media, and a constant fixed pressure is imposed at the fractures. The matrix–fracture exchange rates are considered as the matching data. We will change various coarse grid triple-porosity parameters to calibrate the transfer rates from the fine grid simulations.

The fine grid model of matrix/fracture transfer with a block size of 20×20 m presented in Section 3.2 is used as reference here for the calibration of the triple porosity model. The number of MINC discretization volumes used is the same than the one used for the upscaling of the matrix/fracture interaction for a bulk fluid in a dual porosity with MINC discretization in Section 4.1. The number of MINC volumes used in the triple porosity model is then ten. The large pore medium corresponds to the volume fraction of the matrix without confinement effect on the fluid. On the contrary the small pore medium includes a flash with capillary pressure to take into account the confinement effect on the fluid inside nanopores. Therefore the large pore medium corresponds to the Facies 3 of the fine grid model and the small pores medium corresponds to the Facies 1 and 2 of the fine grid model. The properties of the three Facies are summarized in Table 6 in Section 3.2. Each distribution 'D' have different volume fraction of the three Facies (Table 7). The volume of large pore and small pore
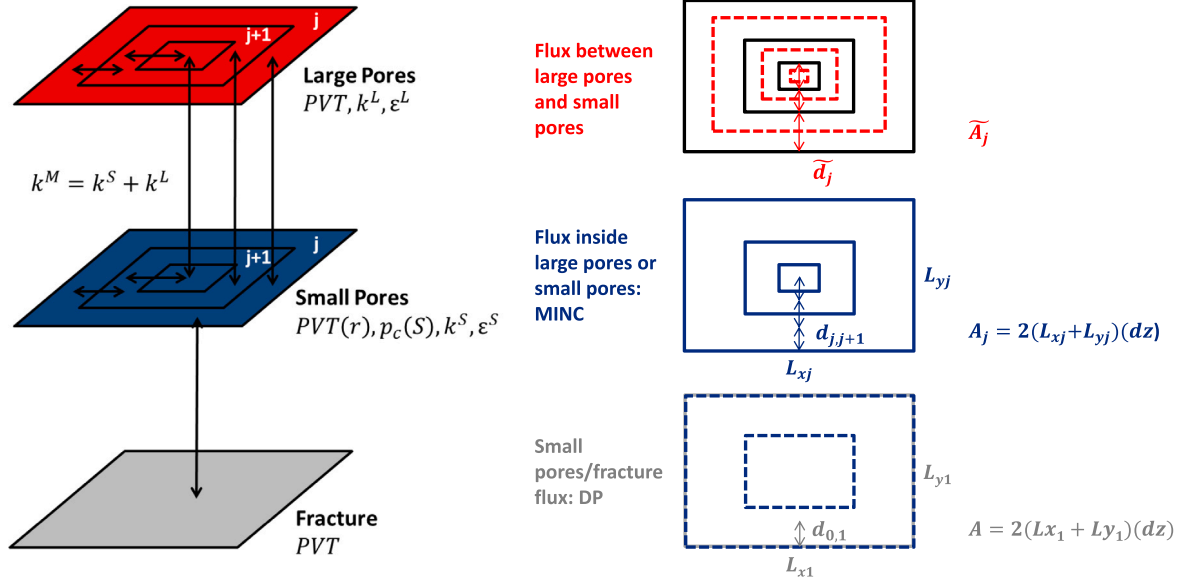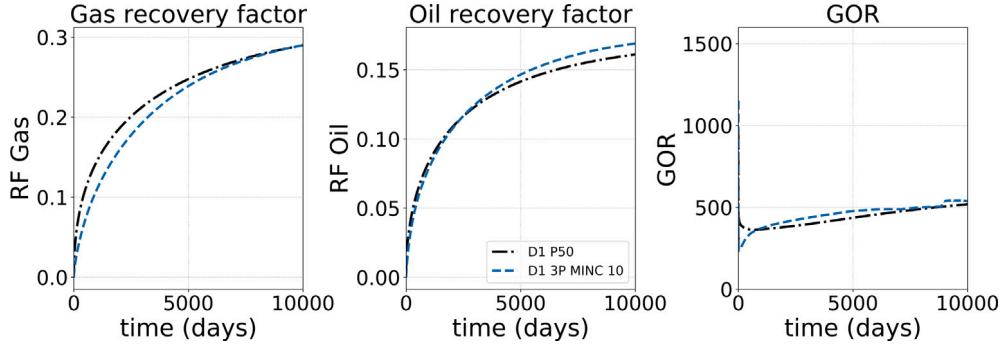
Fig. 17. Schematic of triple porosity model discretization for one matrix/fracture block.

Fig. 18. Calibration of D1 for block size 20 × 20 m. The black curve corresponds to the fine grid results and the blue curve correspond to the triple porosity model results. The graphs represent gas recovery factor versus time (left), oil recovery factor versus time (center) and gas–oil ratio versus time (right). (For interpretation of the references to color in this figure legend, the reader is referred to the web version of this article.)

media must therefore be adapted for each distributions. The system of Eqs. (28) below gives the large pore and small pore volumes and porosities as a function of the matrix properties. The porous volume of the matrix and the volume fraction of each Facies are conserved.

$$
\begin{cases}
\epsilon^M V^M = \epsilon^L V^L + \epsilon^S V^S \\
\epsilon^M = \epsilon_1 v_{f1} + \epsilon_2 v_{f2} + \epsilon_3 v_{f3} \\
\epsilon^S = \dfrac{\epsilon_1 v_{f1} + \epsilon_2 v_{f2}}{v_{f1} + v_{f2}} \\
\epsilon^L = \epsilon_3 \\
V^L = v_{f3} V^M \\
V^S = (v_{f1} + v_{f2}) V^M
\end{cases}
\tag{28}
$$

where $\epsilon^M, \epsilon^L, \epsilon^S$ are the porosities of the matrix, large pore and small pore medium respectively. V^M, V^L, V^S are the volumes of the matrix, large pore and small pore medium respectively. v_{f1}, v_{f2}, v_{f3} are the volume fractions of the Facies 1, 2, 3 respectively. Their values for each distribution 'D' are given in Table 7 in Section 3.2.

To reduce the number of calibration parameters, we assume that the flow between large pores and small pores is parallel. That means that the permeability of the matrix is equal to the sum of the permeabilities of small pores and large pores.

$$
k^M = k^L + k^S
\tag{29}
$$

Here, the large pore permeability k^L reflects the connection between large pores, which are in reality separated by small pores. It is also possible that there are not direct connection between them. Other assumptions can also be used, for example, the weighted harmonic average: $\frac{V^M}{k^M} = \frac{V^L}{k^L} + \frac{V^S}{k^S}$, but this relation is not tested in this work.

Several calibration parameters are considered in the triple porosity model in order to match the fine grid production results. The main parameters are firstly the pore radius r used in the flash with capillary pressure (Section 2.1) performed in the small pore medium. Secondly, the pore structure parameter α in the flux between large pore and small pore media Eq. (25). Moreover, the permeability of the large pore medium k^L which gives the permeability in small pores medium k^S thanks to Eq. (29). The small pore medium gathers Facies 1 and 2 which includes pores from 2 to 100 nm. The effect of confinement is very low for pore radius higher than 50 nm (see Fig. 8 in Section 3.3), so a volume fraction of fluid in the small pore medium may behave almost like a fluid in large pore medium without confinement effect. Therefore the volume fraction of large pores medium v_{f3} is also considered as a calibration parameter v_L. In order to respect the pore volume conservation of matrix, the porosity of the large pores medium is calculated by:

$$
\epsilon^L = \frac{\epsilon^M - (1 - v_L)\epsilon^S}{v_L}
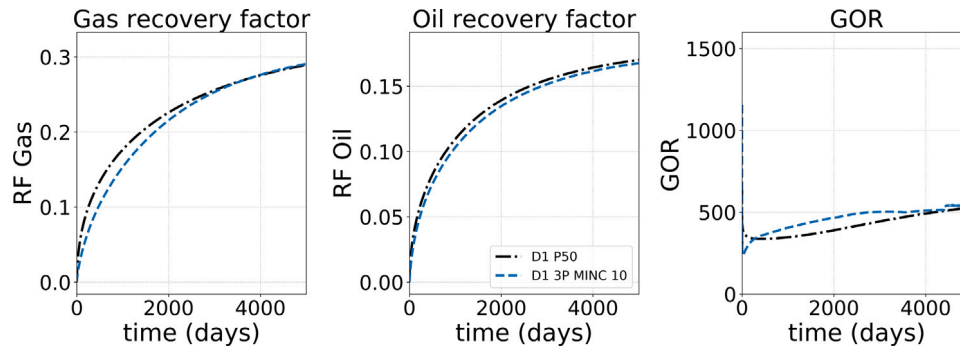\tag{30}
$$

Fig. 19. Calibration of D1 for block size 10 × 40 m. The black curve corresponds to the fine grid results and the blue curve correspond to the triple porosity model results. The graphs represent gas recovery factor versus time (left), oil recovery factor versus time (center) and gas–oil ratio versus time (right). (For interpretation of the references to color in this figure legend, the reader is referred to the web version of this article.)

Table 10
Calibration parameters of the triple porosity model.

Calibration parameter	Meaning
r	Pore radius used in the flash with capillary pressure performed in the small pore medium
α	Pore structure parameter used in the transmissibility between large pore and small pore media (Eq. (25))
k^L	Permeability of the large pore medium which is linked to k^S (Eq. (29))
v_L	Large pore volume fraction in the matrix which is linked to ϵ^L (Eq. (30))

Table 11
Calibration parameters.

PSD	r (nm)	k^L (nD)	α	v_L (%)	ϵ^L
D1	60	60	0.06	70	0.1
D2	6	60	0.08	59	0.1
D3	5	30	0.21	40	0.1
D4	7	0	0.14	40	0.0848
D5	10	0	0.08	40	0.061

with $\epsilon^S = \frac{\epsilon_1 v_{f1} + \epsilon_2 v_{f2}}{v_{f1} + v_{f2}}$. So the porous volume of the matrix block is unchanged, because $\epsilon^L V^L + \epsilon^S V^S = \epsilon^L v_L V^M + \epsilon^S (1 - v_L) V^M$. We replace ϵ^L by Eq. (30) and we find $\epsilon^L V^L + \epsilon^S V^S = \epsilon^M V^M$.

In conclusion there are four calibration parameters. Firstly, the average pore radius used in the small pore medium flash r. Secondly, the pore structure parameter α used in the transmissibility between large pore and small pore media. Afterwards, the large pore permeability k^L, which reflects the connection between different large pores. Finally, the large pore volume fraction v_L which is linked to the large pore porosity ϵ^L by the system of Eqs. (30). The different parameters are summarized Table 10.

4.3.2. Numerical example

A calibration of the triple porosity model using the four calibrations parameters as variables has been performed for each of the five distributions 'D'. The values of the calibration parameters which allow to get a good match with the fine grid production results are summarized Table 11 for every distributions 'D'. A certain logic is observed in the evolution of calibration parameters versus the increasing volume fraction of nano-pores from D1 to D5. The pore radius decreases from D1 to D3 because the radius is representative of the volume fraction of nano-pores in the matrix. The large pore medium permeability decreases from D1 to D5 because at fine scale the volume of large pores surrounded by small pores decreases. Therefore in the triple porosity model the fluid can flow directly from large pores to small pores without internal flow inside large pore medium. The average pore structure parameter α depends on the PSD and the contact area between large and small pores. The large pore volume fraction is not used as a fitting parameter from D1 to D3, it is equal to the volume fraction of Facies 3 v_{f3}. The large pore volume fraction is increased for D4 and D5 in order to take into account the volume fraction of small pores with relatively large radius whose fluid behaves like bulk. The evolution of the different calibration parameters is not monotonic from D1 to D5 because the large pore volume fraction of D4 and D5 is modified.

The comparison between the calibrated triple porosity model and the fine grid production results for the distribution D1 is given Fig. 18.

It corresponds to the simulation case with a matrix block size of 20 × 20 m. The results for the others distributions D2, D3, D4, D5 are given Figs. 31 to 34 in Appendix A.3.2. For all the distributions, the match between the triple porosity (3P MINC 10) and the fine grid (P50) production results is very satisfactory.

We believe that the four calibration parameters: r, α, k^L and v_L for the triple porosity model depend mainly on the PSD. They do not depend strongly on the matrix block size and form. In the following, the same calibration parameters summarized in Table 11 have been used for the rectangular matrix/fracture configuration with matrix block sizes of 10 × 40 m. This simulation case has been presented in Section 3.3 and fine grid simulations have been performed.

The comparison of triple porosity and fine grid production results for matrix block size of 10 × 40 m and for distribution D1 is given Fig. 19. The results for the other distributions D2, D3, D4, D5 are given in Appendix A.3.2 Figs. 35 to 38.

The match between the triple porosity model and the fine grid production results are very good for all the distributions and for the different block sizes and matrix/fracture configurations. Given a PSD, only one calibration of the triple porosity model for a given matrix/fracture configuration is necessary to upscale all other matrix/fracture configurations. The triple porosity model developed in this work is therefore efficient and robust. An upscaled model of the matrix/fracture interaction has been fitted for each of the five distributions 'D'. This model does not depend on the matrix/fracture configuration or the matrix block size. A large scale reservoir simulation case can therefore be built with this triple porosity approach.

5. Simulation of a fractured well in a stimulated reservoir volume (SRV)

In the literature, the reservoir simulation for an ultra low permeability reservoir at SRV scale is generally made with a single and a dual porosity model with a discrete pore size distribution of one value per cell or an average pore radius (Firincioglu et al., 2013; Sanaei et al., 2014; Alharthy et al., 2017; Haider and Aziz, 2017; Lopez Jimenez et al., 2018). We propose here to apply the triple porosity model presented above to a large scale reservoir simulation of a horizontal producing well in a SRV.
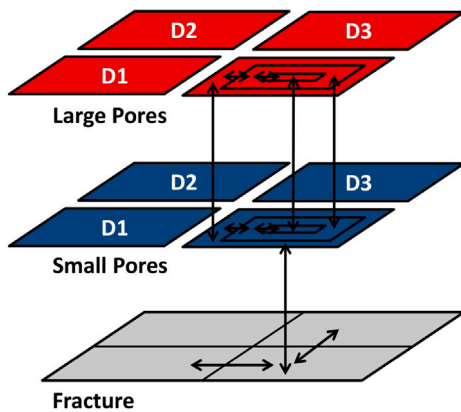
Fig. 20. Schematic of MINC triple porosity model for SRV simulation.

5.1. Reservoir model

The large scale reservoir simulation model is represented in Fig. 20. The flow between cells of the same medium is only possible for the fracture medium as illustrated by the arrows in Fig. 20. F_F^i should therefore not be zero in Eq. (17). The flux between a given cell of the fracture medium with its neighboring cells is calculated using Eq. (19). The matrix is considered heterogeneous with different PSD inside. Then a spacial distribution of the different distributions 'D' has been built. The different calibrated triple porosity model for a given distribution 'D' presented in the previous section for one fracture cell are therefore linked together through the fracture medium according to their spacial coordinates. The different upscaled parameters of the triple porosity models for each distributions 'D' are the same as the one used in previous section in Table 11.

A SRV simulation case has been built according to Fig. 21 with one horizontal well in the center. The 2D grid is 2000 m length and 1300 m width and the cell dimensions in the x, y and z directions are 100x100x10 m. The matrix block size used for the matrix–fracture transfer modeling is 20×20 m. Therefore, there are 5 matrix blocks per cell. The fracture permeability in the well cells is fixed to 100D and the remaining SRV have an equivalent fracture permeability of 0.01D and 0.001D as illustrated in Fig. 21 left. A random realization of the different distributions D1, D2, D3, D4, D5 has been performed in the matrix as illustrated Fig. 21 right. The distribution corresponds to a volume fraction of 15% of D1, 40% of D2, 10% of D3, 15% of D4 and 20% of D5. The simulation setup is the same as the one detailed in Section 3.2. Bakken oil is used for the simulation, the initial pressure in the SRV is 200 bar and the production pressure of the well is fixed to 100 bar. The production from the SRV through the horizontal well is simulated during 10 000 days.

5.2. SRV production results

Fig. 22 represents the production results for bulk fluid in a dual porosity MINC method ("Bulk 2P MINC 10") and for confined fluid. The confined fluid production is modeled by the dual porosity MINC method ("D distribution 2P MINC 10") and the triple porosity model ("D distribution 3P MINC 10"). The "Bulk 2P MINC 10" model corresponds to a dual porosity model with 10 MINC volumes and zero capillary pressure. The classic Peng–Robinson EOS is used and different porosities are assigned in each cell according to the PSD. The "D distribution 2P MINC 10" model corresponds to a dual porosity model with 10 MINC volumes, capillary pressure and pore radius dependent EOS in the matrix. Similarly, different porosities are assigned in each cell (or PSD). The pore radius assigned to each cell corresponds to the one used in the calibrated triple porosity model for the PSD considered.

The confined "D distribution 3P MINC 10" model corresponds to the triple porosity model presented in Section 4.2 with different upscaled parameters for each cell (or PSD) summarized in Table 11. The dual-porosity MINC simulation is usually used in the literature to study tight oil and shale gas reservoirs production with nanopore modified PVT behavior. The differences between the triple-porosity MINC simulation and the dual-porosity MINC simulation are very large (Fig. 22). As observed at matrix/fracture interaction scale, the production results of the "D2 3P MINC 10" model shows higher oil production and lower gas production and GOR than the "Bulk 2P MINC 10" results. This trend observed at fine scale (Section 3.3) and in field observation (Section 1) is not represented by the "D distribution 2P MINC 10" model mostly used in the literature. We therefore believe that the triple porosity approach gives more reliable results, and the dual porosity model is not very accurate to handle the pore size distribution issue.

Pressures and saturation fields have been plotted in Figs. 23, 24 and 25 for a specific time (980 days) in each sub domains of the triple porosity model: fracture (F), small pores (SP) and large pores (LP). The gas saturation is higher in the large pore medium than in the small pore medium. This is due to the bubble point decrease in the small pore medium because of the pore dependent PVT behavior. The gas pressure is higher than the oil pressure only in the small pores medium. Indeed, capillary pressure is equal to zero in large pore, which is not the case in small pores. This difference of capillary pressure participates to slow down the gas flow from large pore medium to fracture through small pore medium where capillary pressure is high. This example shows that the effect of pore size dependent PVT behavior and capillary pressure heterogeneity observed at fine scale (Section 3.3) are taken into account in the triple porosity model.

6. Summary of the model development

The methodology developed in this paper to model unconventional low permeability reservoir production is summarized in Fig. 26. This is a multi-scale approach where the thermodynamic and the flow of the confined fluid has been modeled and studied from nano-pore scale to matrix/fracture scale and finally reservoir scale. From given PSD measured in laboratories for different facies of a reservoir, different fine scale reservoir simulations can be performed for these PSD at matrix block scale. This fine grid simulation includes the modified pore size dependent EOS. These fine grid results are used to calibrate the triple porosity for the different PSD. Then a large scale SRV can be built using the triple porosity model calibrated for the different PSD corresponding to the reservoir facies. Finally we can get accurate production results of the SRV considering fluid confinement.

7. Conclusion

Unconventional low permeability reservoirs are characterized by a very heterogeneous pore size distribution (PSD) and an important volume fraction of nanopores. These particularities modifies the PVT behavior of the fluid and its flow inside the reservoir. Reservoir production are therefore inevitably altered from a conventional reservoir without fluid confinement. This work has therefore proposed a methodology in order to model accurately the flow and the thermodynamic behavior of the fluid in unconventional low permeability reservoir.

Thanks to the reference results from molecular simulation Sobecki et al. (2019), we have highlighted the best pore size dependent thermodynamic flash proposed in the literature. The best match is obtained with a flash with both capillary pressure and critical point shift.

The modified pore size dependent EOS has been included into a reservoir simulator. Reservoir simulations have been performed for different PSD at the matrix block scale with very fine grids. Besides studying the impact of confinement on production, this enables to get reference production results for the development of upscaling methodologies for large scale reservoir simulations. For all the PSD studied,
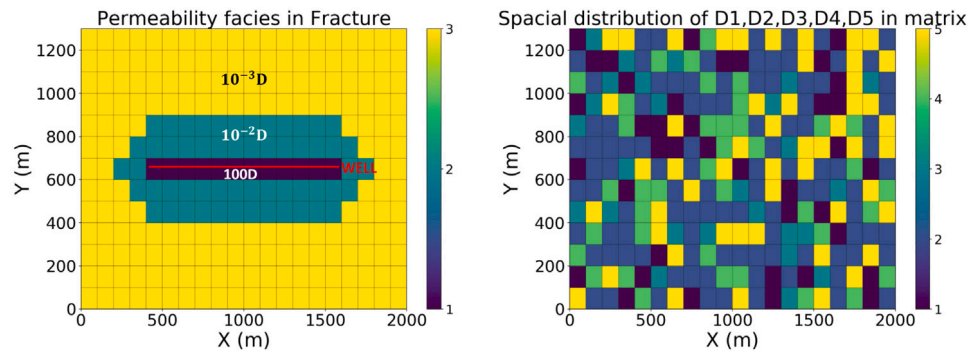
Fig. 21. SRV fracture grid (left) and spacial distribution of D1, D2, D3, D4, and D5 in matrix (right).
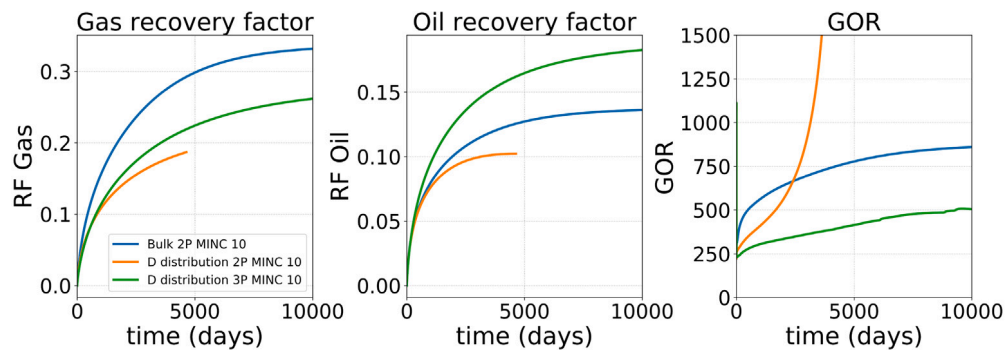

Fig. 22. Production results of the SRV with spacial distribution of D1, D2, D3, D4 and D5. The blue curve corresponds to the results for a bulk fluid using a dual porosity model with 10 MINC volumes. The orange curve corresponds to the results for a confined fluid using a dual porosity model with 10 MINC volumes. The green curve corresponds to the results for a confined fluid using the triple porosity model. The graphs represent gas recovery factor versus time (left), oil recovery factor versus time (center) and gas–oil ratio versus time (right). (For interpretation of the references to color in this figure legend, the reader is referred to the web version of this article.)
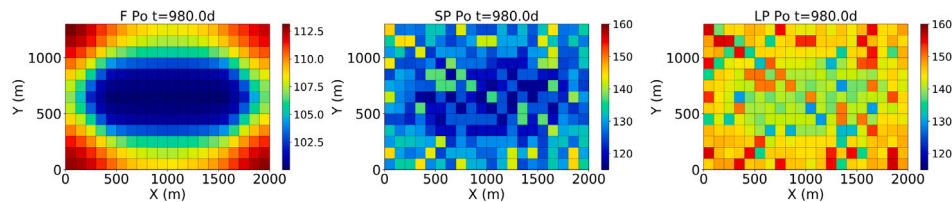
Fig. 23. Oil pressure field in fracture (F) (left), small pore (SP) (center) and large pore (LP) (right) of the triple porosity model at 980 days.
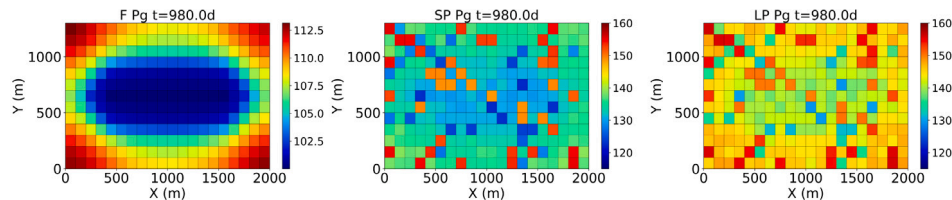
Fig. 24. Gas pressure field in fracture (F) (left), small pore (SP) (center) and large pore (LP) (right) of the triple porosity model at 980 days.
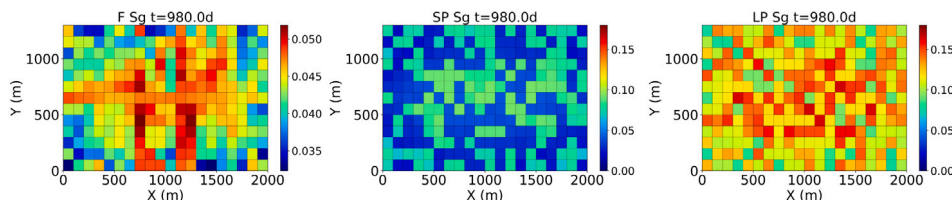
Fig. 25. Gas saturation field in fracture (F) (left), small pore (SP) (center) and large pore (LP) (right) of the triple porosity model at 980 days.

the impact of pore confinement on reservoir production increases the oil production and decreases the gas production and the GOR compared with the bulk fluid. It is manifested by two effects: capillary pressure heterogeneity effect and pore size dependent PVT modeling effect.
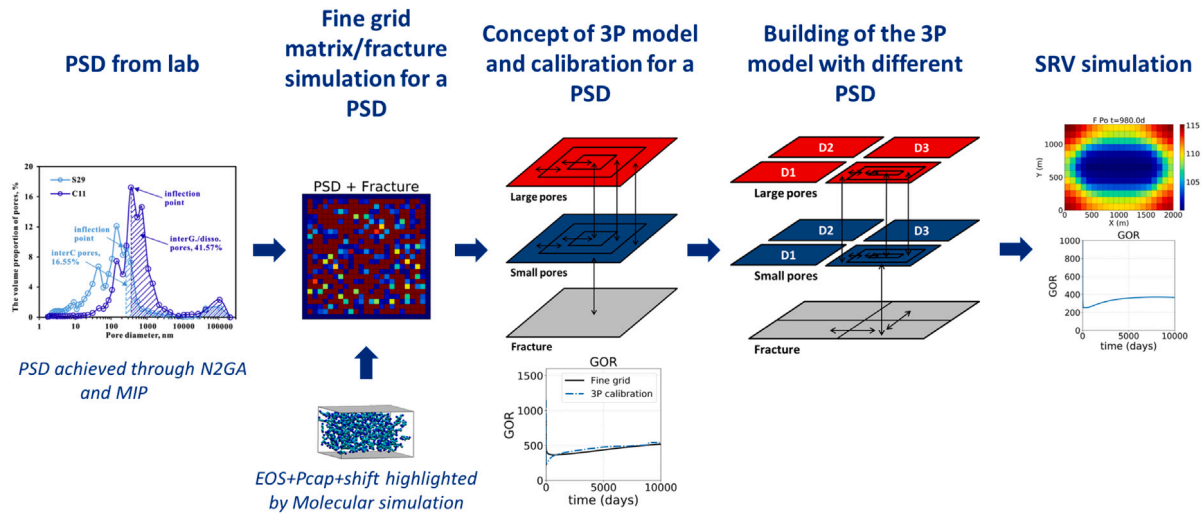
Fig. 26. Schematic of the methodology developed in this paper to model accurately unconventional reservoir including strong PSD heterogeneity and pore size dependent PVT behavior of the fluid.
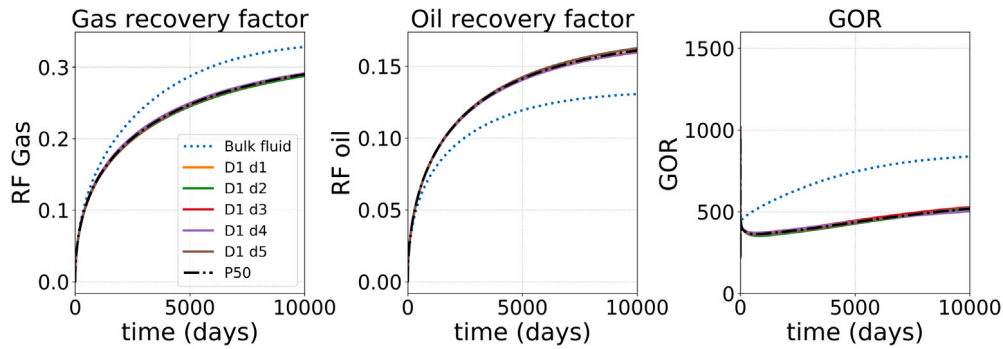*Source:* The left figure comes from Zhang et al. (2016b).

Fig. 27. Production results for the five samples of distribution D1 compared to bulk (block size of 20 × 20 m).
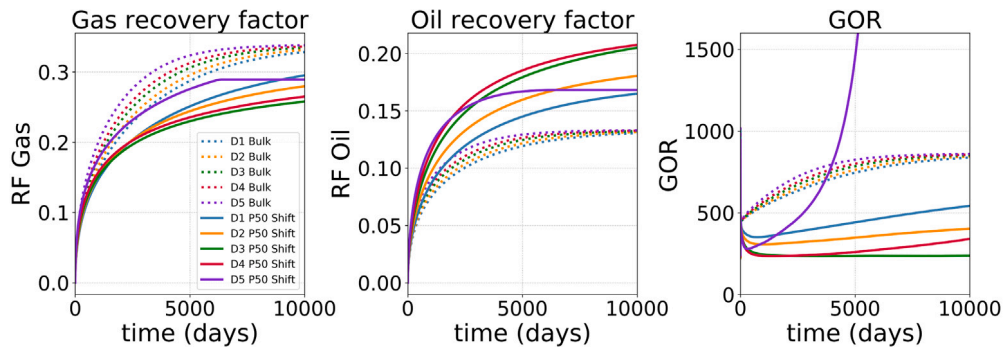

Fig. 28. Comparison of production results for the different distributions for bulk and confined fluid with a flash with critical point shift (block size of 20 × 20 m).

Large scale unconventional low permeability reservoir simulation needs upscaling methodologies because of computational constraints. We have shown that the commonly-used dual porosity MINC model with an average pore radius (whatever the pore radius size) or effective pore radius are unable to match the fine grid results at the matrix block scale. A new triple porosity model has therefore been developed in this paper. Our model considers three domains: fracture, small pores and large pores with their own PVT model and petrophysic properties. Furthermore a MINC discretization is performed in the large pores and small pores media. A calibration of the triple porosity model for several PSD fine grid results have been done using four fitting parameters. The

new triple porosity model built has shown a very good match with fine grid results.

As an application case, a large scale SRV model with heterogeneous PSD has been built using our triple porosity model. The triple porosity approach has shown quite better results, compared to the commonly-used dual porosity models with an equivalent nanopore radius.

We believe that the triple porosity approach is more suitable for the handling of complex physics in nanoporous reservoirs, and gives more reliable results. However, we need to test and validate this model in the future on a discrete fracture network and for 3D flow simulations.
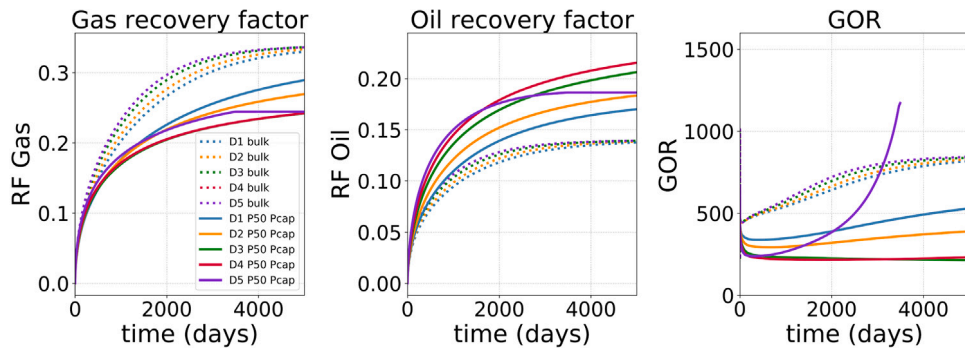
Fig. 29. Comparison of production results for the different distributions for bulk and confined fluid with a flash with capillary pressure for geometry 3 (block size 40 × 10 m).
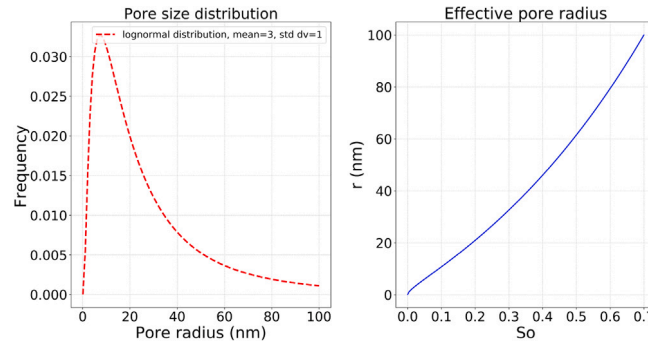

Fig. 30. Example of effective radius for a PSD modeled by a lognormal distribution of mean 3 and standard deviation of 1 for pore sizes between 0 and 100 nm.

CRediT authorship contribution statement

Nicolas Sobecki: Conceptualization, Methodology, Software, Investigation. **Shihao Wang:** Data curation, Validation. **Didier Yu Ding:** Supervision, Investigation. **Carlos Nieto-Draghi:** Supervision, Investigation. **Yu-Shu Wu:** Supervision.

Declaration of competing interest

The authors declare that they have no known competing financial interests or personal relationships that could have appeared to influence the work reported in this paper.

Acknowledgment

Appendix. Appendices

A.1. Thermodynamic modeling of fluid in nanopores Appendices

The fugacity coefficients are calculated from the following expressions:

$$
ln(\Phi_i^l) = \frac{b_i(Z^l - 1)}{b_m} - ln(Z^l - B_m)
$$
$$
- \frac{A_m}{2\sqrt{2}B_m}\left(\frac{2\Psi_i}{(a\alpha)_m} - \frac{b_i}{b_m}\right)ln\left(\frac{Z^l + (1 + \sqrt{2})B_m}{Z^l - (1 - \sqrt{2})B_m}\right) \tag{31}
$$

$$
ln(\Phi_i^v) = \frac{b_i(Z^v - 1)}{b_m} - ln(Z^v - B_m)
$$

$$
- \frac{A_m}{2\sqrt{2}B_m}\left(\frac{2\Psi_i}{(a\alpha)_m} - \frac{b_i}{b_m}\right)ln\left(\frac{Z^v + (1 + \sqrt{2})B_m}{Z^v - (1 - \sqrt{2})B_m}\right) \tag{32}
$$

$$
\Psi_i = \sum_j x_j \sqrt{a_i a_j \alpha_i \alpha_j (1 - k_{ij})} \tag{33}
$$

The variables Z^l and Z^v comes from the Peng–Robinson EOS resolution.

The equilibrium ratio of the component i is defined as: $K_i = \frac{y_i}{x_i}$. By definition, we have: $x_i = \frac{z_i}{L+VK_i}$ and $y_i = \frac{z_i K_i}{L+VK_i}$. Since $\sum_i y_i - \sum_i x_i = 0$, then replacing L by $1 - V$, we get the Rachford–Rice equation:

$$
\sum_i \frac{(K_i - 1)z_i}{1 + V(K_i - 1)} = 0 \tag{34}
$$

This equation allows to calculate V knowing K_i and then x_i and y_i.

The correlation of Meyra et al. (2005) (Eq. (35)) and Bird et al. (2007) Eq. (36) is used to calculate the critical pressure shift function of the pore radius.

$$
\frac{P_{cb} - P_{cp}}{P_{cb}} = 0.9409\frac{\sigma}{r_p} - 0.2415\left(\frac{\sigma}{r_p}\right)^2 \tag{35}
$$

$$
\sigma = 0.244\left(\frac{T_{cb}}{P_{cb}}\right)^{1/3} \tag{36}
$$

with T_{cb}: bulk critical temperature (K), T_{cp}: confined critical temperature (K), P_{cb}: bulk critical pressure (atm), P_{cp}: confined critical pressure (atm), σ: characteristic diameter of the molecules (nm), r_p: pore radius (nm).

Jin et al. (2013) use the results of Singh et al. (2009), Singh and Singh (2011), Vishnyakov et al. (2001) to build the correlations for critical temperature Eq. (37). Sanaei et al. (2014) have adjusted these correlations.

$$
1 - \frac{T_{cp}}{T_{cb}} = 0.8493\left(\frac{2r_p}{\sigma}\right)^{-1.241} + 0.015 \tag{37}
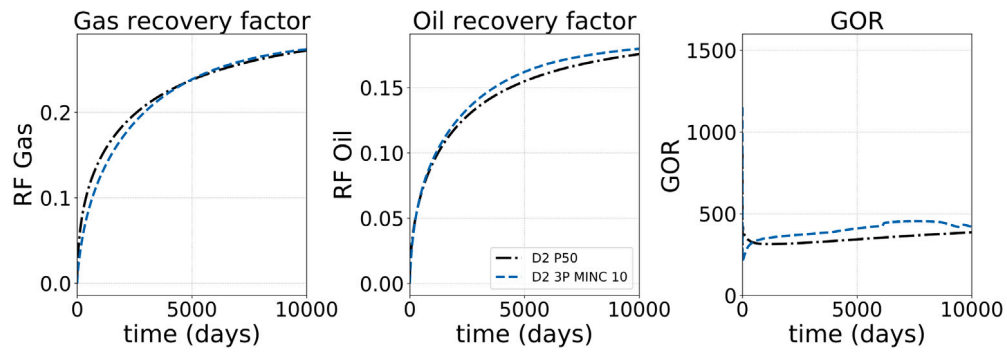$$

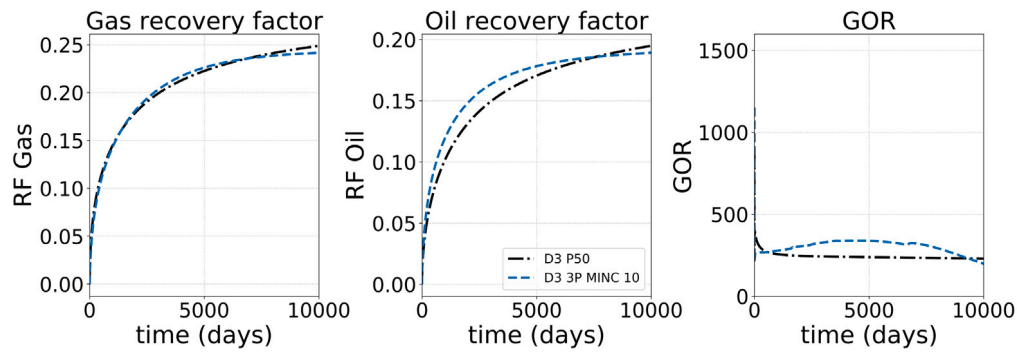**Fig. 31.** Calibration of the triple porosity model for D2 (block size 20 × 20 m).

Fig. 32. Calibration of the triple porosity model for D3 (block size 20 × 20 m).
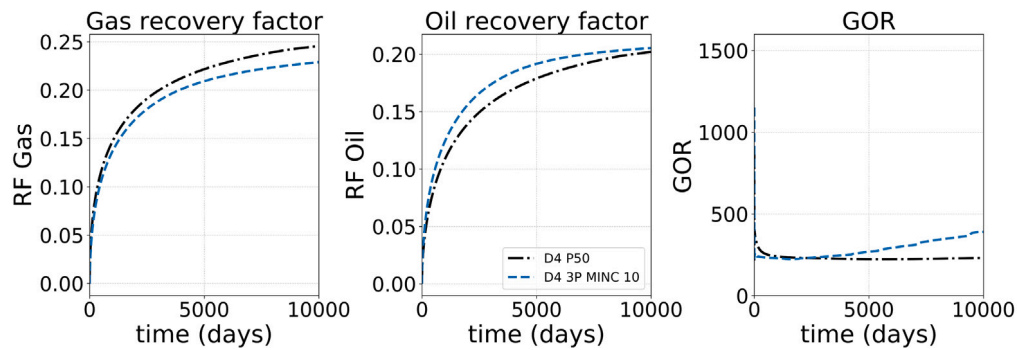
Fig. 33. Calibration of the triple porosity model for D4 (block size 20 × 20 m).
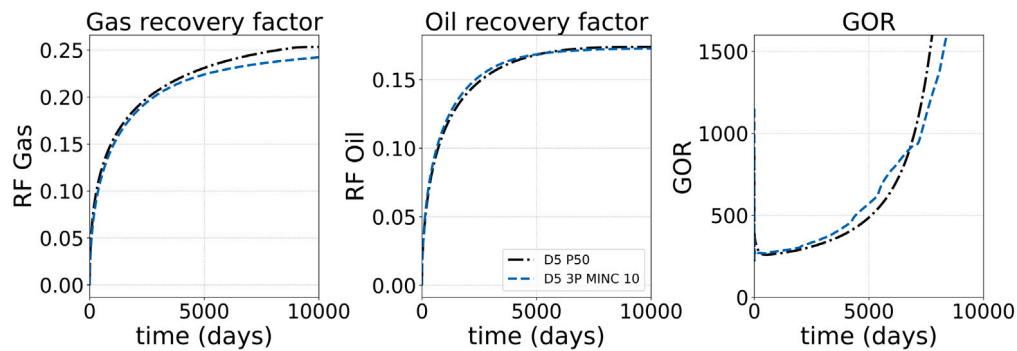
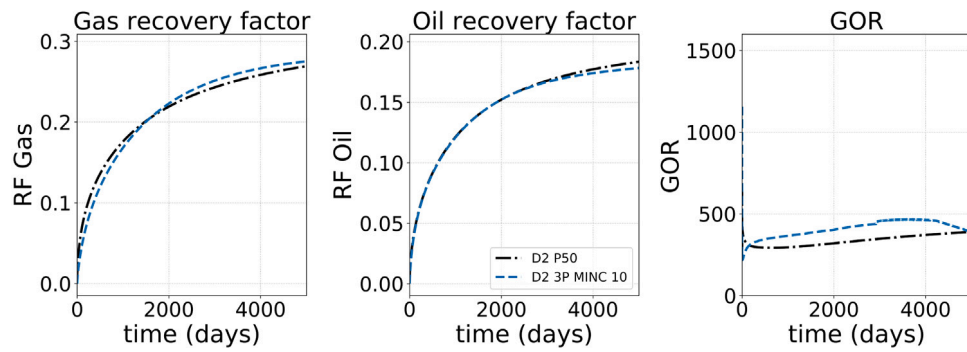**Fig. 34.** Calibration of the triple porosity model for D5 (block size 20 × 20 m).

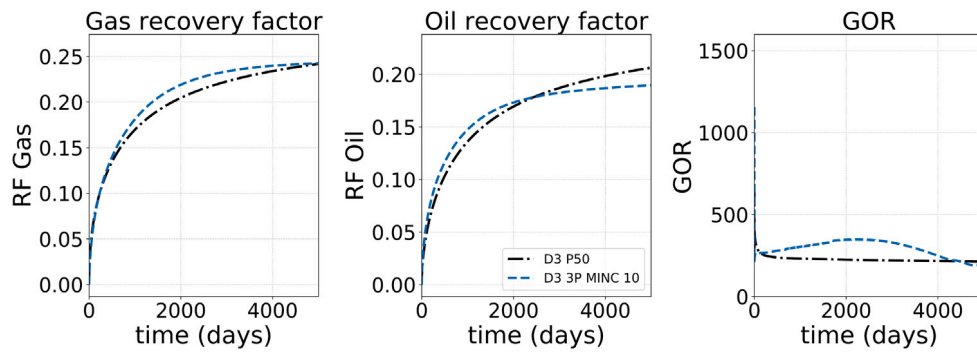**Fig. 35.** Calibration of the triple porosity model for D2 (block size 10 × 40 m).

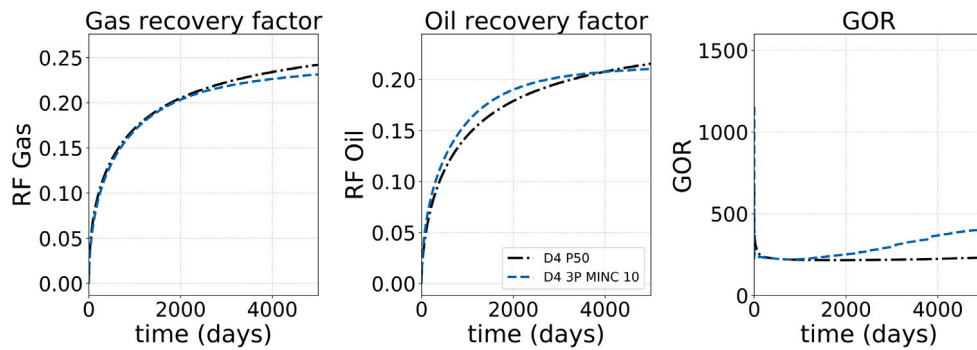**Fig. 36.** Calibration of the triple porosity model for D3 (block size 10 × 40 m).

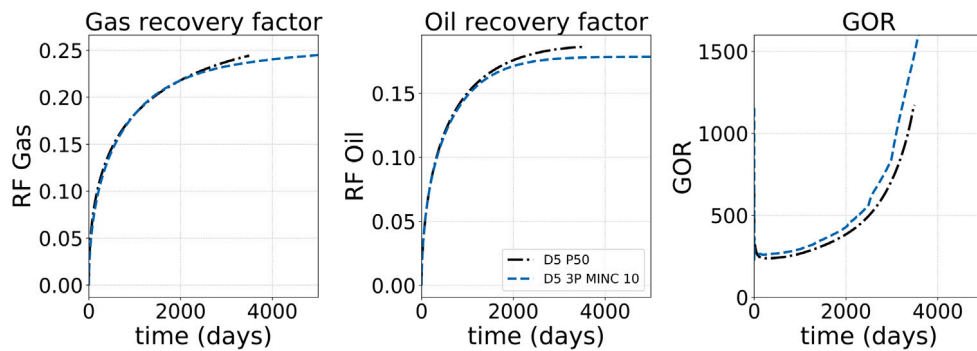**Fig. 37.** Calibration of the triple porosity model for D4 (block size 10 × 40 m).

Fig. 38. Calibration of the triple porosity model for D5 (block size 10 × 40 m).

A.2. Matrix/fracture interaction with pore size distribution Appendices

See Figs. 27–29

A.3. Upscaling for large scale reservoir simulation Appendices

A.3.1. Effective radius

Li et al. (2016), Li and Mezzatesta (2017) considered the effective radius as a function of saturation in the Laplace equation of the flash with capillary pressure. From a pore size distribution, he defined the wetting fluid saturation as following:

$$S_l(r_K) = \frac{\sum_{r_i \le r_K} \Delta V_i(r_i)}{\sum_{r_i} \Delta V_i(r_i)} \tag{38}$$

with S_l: wetting phase saturation, r_K: effective radius, r_i: radius of the pore size distribution, $\Delta V_i(r_i)$: pore volume corresponding to a pore size of r_i

They consider that the pore network is initially filled with oil and all pores are connected, the effective radius is then maximum. When gas appears firstly in larger pores during depletion, gas stays in larger pores and oil stays in smaller pores because of the oil wet characteristic of the rock. Then the effective radius represents the pore size limit between oil and gas phases.

The effective pore radius versus oil saturation is built from a volumetric pore-size distribution. A pore radius size distribution is not always volumetric but a volumetric distribution can be found through a transformation. For example, if capillary tubes are considered, a tube of radius r has a volume $\pi r^2 L$ with L the length of the tubes. Therefore the radius squared distribution allows to obtain the volumetric pore size distribution. In order to move from a probability density function of r to a probability density function of r^2, a transformation is required. Let R be the random variable of the pore radius with $f_r(x)$ as the density function. The probability function of the random variable $U = R^2$ is calculated by:

$$P(U \le u) = P(R^2 \le u) = P(R \le \sqrt{u}) = \int_0^{\sqrt{u}} f_r(x)dx = \int_0^u \frac{f_r(\sqrt{y})}{2\sqrt{y}}dy \tag{39}$$

So, the density function of the squared radius is given by:

$$f_{r^2}(u) = \frac{f_r(\sqrt{u})}{2\sqrt{u}} \tag{40}$$

Then the oil saturation function of the effective radius $S_o(r_K)$ is the normalized cumulative distribution function (CDF) of f_{r^2}. If initial water saturation is taken into account, the general equation is:

$$S_o(r_K) = (1 - S_{wi})\frac{CDF_{f_{r^2}}(r_K)}{CDF_{f_{r^2}}(r_{K\_max})} \tag{41}$$

If spherical pores are considered, the distribution of the random variable $U = R^3$ should be computed. An example of effective radius is shown Fig. 30 for a pore size distribution modeled by a lognormal distribution of mean 3 and standard deviation of 1 for pore sizes between 0 and 100 nm.

A.3.2. Results

See Figs. 31–38

References

Alfi, M., An, C., Cao, Y., Yan, B., Barrufet, M.A., Killough, J.E., 2017. Pore size variability and sieving effect in liquid shale-a multiple permeability approach and eagle ford case study. http://dx.doi.org/10.2118/182643-MS.

Alfi, M., Nasrabadi, H., Banerjee, D., 2016a. Experimental investigation of confinement effect on phase behavior of hexane, heptane and octane using lab-on-a-chip technology. Fluid Phase Equilib. 423, 25–33. http://dx.doi.org/10.1016/j.fluid.2016.04.017.

Alfi, M., Nasrabadi, H., Banerjee, D., 2016b. Experimental investigation of confinement effect on phase behavior of hexane, heptane and octane using lab-on-a-chip technology. Fluid Phase Equilib. 423, 25–33. http://dx.doi.org/10.1016/j.fluid.2016.04.017.

Alharthy, N.S., Nguyen, T., Teklu, T., Kazemi, H., Graves, R., 2013. Multiphase compositional modeling in small-scale pores of unconventional shale reservoirs. In: SPE Annual Technical Conference and Exhibition, 30 September-2 October. SPE, New Orleans, Louisiana, USA, http://dx.doi.org/10.2118/166306-MS.

Alharthy, N.S., Teklu, T.W., Abd El-Gawad, S., Kazemi, H., Graves, R., 2017. Flow dynamics and pore scale physics in unconventional shale reservoirs. In: SPE/AAPG/SEG Unconventional Resources Technology Conference, 24-26 July,. SPE, Austin, Texas, USA, http://dx.doi.org/10.15530/URTEC-2017-2698056.

Barbosa, G.D., Travalloni, L., Castier, M., Tavares, F.W., 2016. Extending an equation of state to confined fluids with basis on molecular simulations. Chem. Eng. Sci. 153, 212–220. http://dx.doi.org/10.1016/j.ces.2016.07.033.

Barenblatt, G., Zheltov, I., Kochina, I., 1960. Basic concepts in the theory of seepage of homogeneous liquids in fissured rocks. J. Appl. Math. Mech. 24 (5), 1286–1303. http://dx.doi.org/10.1016/0021-8928(60)90107-6.

Bi, R., Nasrabadi, H., 2019. Molecular simulation of the constant composition expansion experiment in shale multi-scale systems. Fluid Phase Equilib. 495, 59–68. http://dx.doi.org/10.1016/j.fluid.2019.04.026.

Bird, R.B., Stewart, W.E., Lightfoot, E.N., 2007. Transport Phenomena, Vol. 1, Revised second ed. John Wiley & Sons Inc, New York etc..

BP, 2017. BP energy outlook. URL: https://www.bp.com/content/dam/bp/pdf/energy-economics/energy-outlook-2017/bp-energy-outlook-2017.pdf. (accessed January 2019).

Cho, H., Bartl, M.H., Deo, M., 2017. Bubble point measurements of hydrocarbon mixtures in mesoporous media. Energy Fuels 31 (4), 3436–3444. http://dx.doi.org/10.1021/acs.energyfuels.6b02424.

Devegowda, D., Sapmanee, K., Civan, F., Sigal, R.F., 2012. Phase behavior of gas condensates in shales due to pore proximity effects: Implications for transport, reserves and well productivity. In: SPE Annual Technical Conference and Exhibition, 8-10 October. SPE, San Antonio, Texas, USA, http://dx.doi.org/10.2118/160099-MS.

Dong, X., Liu, H., Hou, J., Chen, Z., 2016a. Phase behavior of hydrocarbon mixtures in the organic nanopores of unconventional gas condensate reservoirs. In: SPE/AAPG/SEG Unconventional Resources Technology Conference, 1-3 August. URTEC, San Antonio, Texas, USA, http://dx.doi.org/10.15530/URTEC-2016-2460485.

Dong, X., Liu, H., Hou, J., Wu, K., Chen, Z., 2016b. Phase equilibria of confined fluids in nanopores of tight and shale rocks considering the effect of capillary pressure and adsorption film. Ind. Eng. Chem. Res. 55 (3), 798–811. http://dx.doi.org/10.1021/acs.iecr.5b04276.

ExxonMobil, 2018. Outlook for energy: A view to 2040. URL: https://corporate.exxonmobil.com/-/media/Global/Files/outlook-for-energy/2018-Outlook-for-Energy.pdf. (accessed January 2019).

Firincioglu, T., Ozgen, C., Ozkan, E., 2013. An excess-bubble-point-suppression correlation for black oil simulation of nano-porous unconventional oil reservoirs. In: SPE Annual Technical Conference and Exhibition, 30 September-2 October. SPE, New Orleans, Louisiana, USA, http://dx.doi.org/10.2118/166459-MS.

Firincioglu, T., Ozkan, E., Ozgen, C., 2012. Thermodynamics of multiphase flow in unconventional liquids-rich reservoirs. In: SPE Annual Technical Conference and Exhibition, 8-10 October. SPE, San Antonio, Texas, USA, http://dx.doi.org/10.2118/159869-MS.

Gelb, L.D., Gubbins, K.E., Radhakrishnan, R., Sliwinska-Bartkowiak, M., 1999. Phase separation in confined systems. Rep. Progr. Phys. 62 (12), 1573. http://dx.doi.org/10.1088/0034-4885/62/12/201.

Haider, B.A., Aziz, K., 2017. Impact of capillary pressure and critical property shift due to confinement on hydrocarbon production in shale reservoirs. In: SPE Reservoir Simulation Conference, 20-22 February. SPE, Montgomery, Texas, USA, http://dx.doi.org/10.2118/182603-MS.

Islam, A.W., Sun, A.Y., 2017. A theory-based simple extension of peng–robinson equation of state for nanopore confined fluids. J. Pet. Explor. Prod. Technol. 7 (4), 1197–1203. http://dx.doi.org/10.1007/s13202-016-0306-y.

Jiang, S., Gubbins, K.E., 1995. Vapour-liquid equilibria in two-dimensional lennard-jones fluids: unperturbed and substrate-mediated films. Mol. Phys. 86 (4), 599–612. http://dx.doi.org/10.1080/00268979500102221.

Jin, B., Bi, R., Nasrabadi, H., 2017. Molecular simulation of the pore size distribution effect on phase behavior of methane confined in nanopores. Fluid Phase Equilib. 452 (Supplement C), 94–102. http://dx.doi.org/10.1016/j.fluid.2017.08.017.

Jin, L., Ma, Y., Jamili, A., 2013. Investigating the effect of pore proximity on phase behavior and fluid properties in shale formations. In: Annual Technical Conference and Exhibition, 30 September-2 October. SPE, New Orleans, Louisiana, USA, http://dx.doi.org/10.2118/166192-MS.

Khoshghadam, M., Khanal, A., Yu, C., Rabinejadgangi, N., J. Lee, W., 2017. Producing gas-oil ratio behavior of unconventional volatile-oil reservoirs, and its application in production diagnostics and decline curve analysis. In: Unconventional Resources Technology Conference, July 24. SPE, http://dx.doi.org/10.15530/URTEC-2017-2670925.

Kuila, U., Prasad, M., 2011. Understanding pore-structure and permeability in shales. In: ATCE Conference, 30 October-2 November. SPE, Denver, Colorado, USA, http://dx.doi.org/10.2118/146869-MS.

Kuila, U., Prasad, M., 2013. Specific surface area and pore–size distribution in clays and shales. Geophys. Prospect. 61 (2), 341–362. http://dx.doi.org/10.1111/1365-2478.12028.

Kumar, S., 2007. Upper and Lower Bakken shale production contribution to the Middle Bakken reservoir (Ph.D. thesis). Colorado School of Mines. Arthur Lakes Library.

Kumar, S., Hoffman, T., Prasad, M., 2013. Upper and lower bakken shale production contribution to the middle bakken reservoir. In: URTEC Conference, 12-14 August. SPE, Denver, Colorado, http://dx.doi.org/10.1190/urtec2013-001.

Li, B., Mezzatesta, A., 2017. Evaluation of pore size distribution effects on phase behavior of hydrocarbons produced in shale gas condensate reservoirs. In: SPE Middle East Oil and Gas Show and Conference, 6-9 March. Manama, Kingdom of Bahrain. http://dx.doi.org/10.2118/183833-MS.

Li, B., Mezzatesta, A., Li, Y., Ma, Y., Jamili, A., 2016. A multilevel iterative method to quantify effects of pore-size distribution on phase equilibrium of multicomponent fluids in unconventional plays. Petrophysics 57 (02).

Li, Y., Yu, Y., Zheng, Y., Li, J., 2012. Vapor-liquid equilibrium properties for confined binary mixtures involving co2, ch4, and n2 from gibbs ensemble monte carlo simulations. Sci. China Chem. 55 (9), 1825–1831. http://dx.doi.org/10.1007/s11426-012-4724-5.

Liu, J., Bodvarsson, G.S., Wu, Y.-S., 2003. Analysis of flow behavior in fractured lithophysal reservoirs. J. Contam. Hydrol. 62–63, 189–211. http://dx.doi.org/10.1016/S0169-7722(02)00169-9.

Liu, Y., Jin, Z., Li, H.A., 2018. Comparison of peng-robinson equation of state with capillary pressure model with engineering density-functional theory in describing the phase behavior of confined hydrocarbons. In: Society of Petroleum Engineers. SPE Journal, http://dx.doi.org/10.2118/187405-PA.

Lohrenz, J., Bray, B.G., Clark, C.R., 1964. Calculating Viscosities of Reservoir Fluids From Their Compositions. SPE, http://dx.doi.org/10.2118/915-PA.

Lopez Jimenez, B.A., Hernandez, G., Czernia, B., Killough, J.E., Barrufet, M.A., 2018. Effects of thermodynamic and rock properties on the performance of liquids-rich nano-porous shale reservoirs. In: SPE Argentina Exploration and Production of Unconventional Resources Symposium, 14-16 August. SPE, Neuquen, Argentina, http://dx.doi.org/10.2118/191813-MS.

Luo, S., Jin, B., Lutkenhaus, J.L., Nasrabadi, H., 2019. A novel pore-size-dependent equation of state for modeling fluid phase behavior in nanopores. Fluid Phase Equilib. 498, 72–85. http://dx.doi.org/10.1016/j.fluid.2019.06.009.

Luo, S., Nasrabadi, H., Lutkenhaus, J.L., 2016. Effect of confinement on the bubble points of hydrocarbons in nanoporous media. AIChE J. 62 (5), 1772–1780. http://dx.doi.org/10.1002/aic.15154.

Meyra, A.G., Zarragoicoechea, G.J., Kuz, V.A., 2005. Thermodynamic equations for a confined fluid at nanometric scale. Fluid Phase Equilib. 230 (1–2), 9–14. http://dx.doi.org/10.1016/j.fluid.2004.10.014.

Nelson, P.H., 2009. Pore-throat sizes in sandstones, tight sandstones, and shales. AAPG Bull. 93 (3), 329–340. http://dx.doi.org/10.1306/10240808059.

Nojabaei, B., Johns, R.T., Chu, L., 2013. Effect of capillary pressure on phase behavior in tight rocks and shales. SPE Reserv. Eval. Eng. 16 (03), 281–289. http://dx.doi.org/10.2118/159258-PA.

Panagiotopoulos, A.Z., 1987a. Adsorption and capillary condensation of fluids in cylindrical pores by monte carlo simulation in the gibbs ensemble. Mol. Phys. 62 (3), 701–719. http://dx.doi.org/10.1080/00268978700102501.

Panagiotopoulos, A.Z., 1987b. Direct determination of phase coexistence properties of fluids by monte carlo simulation in a new ensemble. Mol. Phys. 61 (4), 813–826. http://dx.doi.org/10.1080/00268978700101491.

Panagiotopoulos, A., Quirke, N., Stapleton, M., Tildesley, D., 1988. Phase equilibria by simulation in the gibbs ensemble. Mol. Phys. 63 (4), 527–545. http://dx.doi.org/10.1080/00268978800100361.

Pathak, M., Cho, H., Deo, M., 2017. Experimental and molecular modeling study of bubble points of hydrocarbon mixtures in nanoporous media. Energy Fuels 31, http://dx.doi.org/10.1021/acs.energyfuels.6b02422.

Péneloux, A., Rauzy, E., Fréze, R., 1982. A consistent correction for redlich-kwong-soave volumes. Fluid Phase Equilib. 8 (1), 7–23. http://dx.doi.org/10.1016/0378-3812(82)80002-2.

Peng, D.-Y., Robinson, D.B., 1976. A new two-constant equation of state. Ind. Eng. Chem. Fundam. 15 (1), 59–64. http://dx.doi.org/10.1021/i160057a011.

Pitakbunkate, T., Balbuena, P.B., Moridis, G.J., Blasingame, T.A., 2016. Effect of confinement on pressure/volume/temperature properties of hydrocarbons in shale reservoirs. SPE J. 21 (02), 621–634. http://dx.doi.org/10.2118/170685-PA.

Pitakbunkate, T., Blasingame, T.A., Moridis, G.J., Balbuena, P.B., 2017. Phase behavior of methane–ethane mixtures in nanopores. Ind. Eng. Chem. Res. 56 (40), 11634–11643. http://dx.doi.org/10.1021/acs.iecr.7b01913.

Pommer, M.E., 2014. Quantitative Assessment of Pore Types and Pore Size Distribution Across Thermal Maturity, Eagle Ford Formation, South Texas (Ph.D. thesis). The University of Texas at Austin.

Pruess, K., 1985. A Practical Method for Modeling Fluid and Heat Flow in Fractured Porous Media. Society of Petroleum Engineers, http://dx.doi.org/10.2118/10509-PA.

Pruess, K., Karasaki, K., 1982. Proximity Functions for Modeling Fluids and Heat Flow in Reservoirs with Stochastic Fracture Distributions. Lawrence Berkeley Lab., Stanford, CA (USA), CA, USA, submitted to the geothermal reservoir engineering workshop, http://doi.org/.

Rezaveisi, M., Sepehrnoori, K., Pope, G.A., Johns, R.T., 2015. Compositional simulation including effect of capillary pressure on phase behavior. In: Annual Technical Conference and Exhibition, 28-30 September. SPE, Houston, Texas, USA, http://dx.doi.org/10.2118/175135-MS.

Sanaei, A., Jamili, A., Callard, J., 2014. Effect of pore size distribution and connectivity on phase behavior and gas condensate production from unconventional resources. In: SPE Unconventional Resources Conference, 1-3 April. SPE, The Woodlands, Texas, USA, http://dx.doi.org/10.2118/168970-MS.

Sandoval, D.R., Yan, W., Michelsen, M.L., Stenby, E.H., 2016. The phase envelope of multicomponent mixtures in the presence of a capillary pressure difference. Ind. Eng. Chem. Res. 55 (22), 6530–6538. http://dx.doi.org/10.1021/acs.iecr.6b00972.

Shapiro, A., Stenby, E.H., 2001. Thermodynamics of the multicomponent vapor-liquid equilibrium under capillary pressure difference. Fluid Phase Equilib. 178 (1–2), 17–32. http://dx.doi.org/10.1016/S0378-3812(00)00403-9.

Singh, S.K., Singh, J.K., 2011. Effect of pore morphology on vapor–liquid phase transition and crossover behavior of critical properties from 3d to 2d. Fluid Phase Equilib. 300 (1–2), 182–187. http://dx.doi.org/10.1016/j.fluid.2010.10.014.

Singh, S.K., Sinha, A., Deo, G., Singh, J.K., 2009. Vapor–liquid phase coexistence, critical properties, and surface tension of confined alkanes. J. Phys. Chem. C 113 (17), 7170–7180. http://dx.doi.org/10.1021/jp8073915.

Sobecki, N., Nieto-Draghi, C., Lella, A.D., Ding, D.Y., 2019. Phase behavior of hydrocarbons in nano-pores. Fluid Phase Equilib. 497, 104–121. http://dx.doi.org/10.1016/j.fluid.2019.05.025.

Stimpson, B.C., Barrufet, M.A., 2016. Effects of confined space on production from tight reservoirs. In: Annual Technical Conference and Exhibition, 26-28 September. SPE, Dubai, UAE, http://dx.doi.org/10.2118/181686-MS.

Teklu, T.W., Alharthy, N., Kazemi, H., Yin, X., Graves, R.M., AlSumaiti, A.M., 2014. Phase behavior and minimum miscibility pressure in nanopores. SPE Reserv. Eval. Eng. 17 (03), 396–403. http://dx.doi.org/10.2118/168865-PA.

Tian, Y., Ayers, W.B., McCain, W.D., 2013. The eagle ford shale play, south texas: Regional variations in fluid types, hydrocarbon production and reservoir properties. In: International Petroleum Technology Conference, 26-28 March. IPTC, Beijing, China, http://dx.doi.org/10.2523/IPTC-16808-MS.

Travalloni, L., Castier, M., Tavares, F.W., 2014. Phase equilibrium of fluids confined in porous media from an extended peng–robinson equation of state. Fluid Phase Equilib. 362, 335–341. http://dx.doi.org/10.1016/j.fluid.2013.10.049.

Travalloni, L., Castier, M., Tavares, F.W., Sandler, S.I., 2010. Critical behavior of pure confined fluids from an extension of the van der waals equation of state. J. Supercrit. Fluids 55 (2), 455–461. http://dx.doi.org/10.1016/j.supflu.2010.09.008.

U.S. Energy Information Administration, 2016. International energy outlook 2016. URL: https://www.eia.gov/outlooks/ieo/pdf/0484(2016).pdf. (accessed January 2019).

U.S. Energy Information Administration, 2017. International energy outlook 2017. URL: https://www.eia.gov/outlooks/ieo/pdf/0484(2017).pdf. (accessed January 2019).

Vishnyakov, A., Piotrovskaya, E.M., Brodskaya, E.N., Votyakov, E.V., Tovbin, Y.K., 2001. Critical properties of lennard-jones fluids in narrow slit-shaped pores. Langmuir 17 (14), 4451–4458. http://dx.doi.org/10.1021/la001641a.

Wang, L., Parsa, E., Gao, Y., Ok, J.T., Neeves, K., Yin, X., Ozkan, E., 2014. Experimental study and modeling of the effect of nanoconfinement on hydrocarbon phase behavior in unconventional reservoirs. In: SPE Western North American and Rocky Mountain Joint Meeting, 17-18 April. Denver, Colorado. http://dx.doi.org/10.2118/169581-MS.

Wang, S., Pomerantz, A.E., Xu, W., Lukyanov, A., Kleinberg, R.L., Wu, Y.-S., 2017a. The impact of kerogen properties on shale gas production: A reservoir simulation sensitivity analysis. J. Natural Gas Sci. Eng. 48, 13–23. http://dx.doi.org/10.1016/j.jngse.2017.06.009.

Wang, F.P., Reed, R.M., 2009. Pore networks and fluid flow in gas shales. In: ATCE, 4-7 October. Society of Petroleum Engineers, New Orleans, Louisiana, http://dx.doi.org/10.2118/124253-MS.

Wang, C., Xiong, Y., Huang, Z., Winterfeld, P., Ding, D., Wu, Y.-S., 2017b. Multi-porosity, multi-physics model to simulate fluid flow in unconventional reservoirs. In: SPE Reservoir Simulation Conference, 20-22 February. Society of Petroleum Engineers, Montgomery, Texas, USA, http://dx.doi.org/10.2118/182698-MS.

Wang, Y., Yan, B., Killough, J., 2013. Compositional modeling of tight oil using dynamic nanopore properties. In: SPE Annual Technical Conference and Exhibition, 30 September-2 October. New Orleans, Louisiana, USA. http://dx.doi.org/10.2118/166267-MS.

Warren, J.E., Root, P.J., 1963. The behavior of naturally fractured reservoirs. SPE (03), 245–255. http://dx.doi.org/10.2118/426-PA.

Whitson, C.H., Michelsen, M.L., 1989. The negative flash. Fluid Phase Equilib. 53, 51–71. http://dx.doi.org/10.1016/0378-3812(89)80072-X.

Wu, Y., 1998. Msflow: Multiphase Subsurface Flow Model of Oil. Gas and Water in Porous and Fractured Media with Water Shutoff Capability. Documentation and User's Guide, Walnut Creek, California.

Wu, Y.-S., Liu, H., Bodvarsson, G., 2004. A triple-continuum approach for modeling flow and transport processes in fractured rock. J. Contam. Hydrol. 73 (1), 145–179. http://dx.doi.org/10.1016/j.jconhyd.2004.01.002.

Wu, Y.-S., Wang, C., Li, J., Fakcharoenphol, P., 2012. Transient gas flow in unconventional gas reservoir. In: SPE Europec/EAGE Annual Conference, 4-7 June. Society of Petroleum Engineers, Copenhagen, Denmark, http://dx.doi.org/10.2118/154448-MS.

Xiong, Y., 2015. Development of a Compositional Model Fully Coupled with Geomechanics and its Application to Tight Oil Reservoir Simulation (Ph.D. thesis). Colorado School of Mines.

Xiong, Y., Winterfeld, P., Wang, C., Huang, Z., Wu, Y.-S., 2015. Effect of large capillary pressure on fluid flow and transport in stress-sensitive tight oil reservoirs. In: Annual Technical Conference and Exhibition, 28-30 September. SPE, Houston, Texas, USA, http://dx.doi.org/10.2118/175074-MS.

Zhang, Y., Lashgari, H.R., Di, Y., Sepehrnoori, K., 2016a. Capillary pressure effect on hydrocarbon phase behavior in unconventional reservoirs. In: SPE Low Perm Symposium, 5-6 May. SPE, Denver, Colorado, USA, http://dx.doi.org/10.2118/180235-MS.

Zhang, L., Lu, S., Xiao, D., Gu, M., 2016b. Characterization of full pore size distribution and its significance to macroscopic physical parameters in tight glutenites. J. Natural Gas Sci. Eng. 38, 434–449. http://dx.doi.org/10.1016/j.jngse.2016.12.026.

Zuo, J.Y., Guo, X., Liu, Y., Pan, S., Canas, J., Mullins, O.C., 2018. Impact of capillary pressure and nanopore confinement on phase behaviors of shale gas and oil. Energy Fuels 32 (4), 4705–4714. http://dx.doi.org/10.1021/acs.energyfuels.7b03975.

Zuo, Y.-X., Stenby, E.H., 1998. Prediction of interfacial tensions of reservoir crude oil and gas condensate systems. SPE J. 3 (02), 134–145. http://dx.doi.org/10.2118/38434-PA.